

Quantum Mechanical and Quasiclassical Trajectory Surface Hopping Studies of the Electronically Nonadiabatic Predissociation of the \tilde{A} State of NaH_2

Michael D. Hack,[†] Ahren W. Jasper,[†] Yuri L. Volobuev,[†] David W. Schwenke,[‡] and Donald G. Truhlar^{*,†}

Department of Chemistry and Supercomputer Institute, University of Minnesota, Minneapolis, Minnesota 55455-0431, and NASA Ames Research Center, Mail Stop 230-3, Moffett Field, California 94035-1000

Received: April 14, 1999; In Final Form: May 28, 1999

Fully coupled quantum mechanical scattering calculations and adiabatic uncoupled bound-state calculations are used to identify Feshbach funnel resonances that correspond to long-lived exciplexes in the \tilde{A} state of NaH_2 , and the scattering calculations are used to determine their partial and total widths. The total widths determine the lifetimes, and the partial widths determine the branching probabilities for competing decay mechanisms. We compare the quantum mechanical calculations of the resonance lifetimes and the average final vibrational and rotational quantum numbers of the decay product, $\text{H}_2(\nu', j')$, to trajectory surface hopping calculations carried out by various prescriptions for the hopping event. Tully's fewest switches algorithm is used for the trajectory surface hopping calculations, and we present a new strategy for adaptive stepsize control that dramatically improves the convergence of the numerical propagation of the solution of the coupled classical and quantum mechanical differential equations. We performed the trajectory surface hopping calculations with four prescriptions for the hopping vector that is used for adjusting the momentum at hopping events. These include changing the momentum along the nonadiabatic coupling vector (\mathbf{d}), along the gradient of the difference in the adiabatic energies of the two states (\mathbf{g}), and along two new vectors that we describe as the rotated- \mathbf{d} and the rotated- \mathbf{g} vectors. We show that the dynamics obtained from the \mathbf{d} and \mathbf{g} prescriptions are significantly different from each other, and we show that the \mathbf{d} prescription agrees better with the quantum results. The results of the rotated methods show systematic deviations from the nonrotated results, and in general, the error of the nonrotated methods is smaller. The nonrotated TFS- \mathbf{d} method is thus the most accurate method for this system, which was selected for detailed study precisely because it is more sensitive to the choice of hopping vector than previously studied systems.

1. Introduction

Trajectory surface hopping^{1–20} (TSH) has become clearly established as a practical method for studying electronically nonadiabatic dynamics in molecular systems. One attractive aspect of the method is that it is applicable even to complicated polyatomic systems. Until recently, however, it was not possible to evaluate the accuracy of the method because accurate quantum mechanical dynamics calculations on electronically nonadiabatic processes were intractable. Recently the situation has changed, and we have begun to test TSH methods against accurate quantal calculations.^{9,10,12,17–20} One goal of this work is to delineate the reliability of TSH methods for various classes of systems (strongly coupled, weakly coupled, bimolecular, unimolecular, etc.), and another is to use what we learn to design improved methods. In the present paper, we focus on electronically nonadiabatic unimolecular decay of long-lived excited-state complexes (exciplexes) and we focus on the prescription for the change in momentum during the hopping event.

One problematic aspect of TSH methods is that the potential energy governing the internuclear motion changes discontinuously during a hop, and a corresponding discontinuous change in kinetic energy is required to conserve the total energy. This is problematic because there is no formal prescription for the

method used to adjust the individual components of the kinetic energy. Two common prescriptions are to adjust the component of the momentum that lies along the nonadiabatic coupling vector^{1,2}

$$\mathbf{d}_{ij}(\mathbf{R}) = \langle \phi_i^a(\mathbf{x}; \mathbf{R}) | \nabla_{\mathbf{R}} \phi_j^a(\mathbf{x}; \mathbf{R}) \rangle \quad (1)$$

and to adjust the component of the momentum that lies along the vector of the gradient of the differences in potential energy^{3,4}

$$\mathbf{g}_{ij}(\mathbf{R}) = \nabla_{\mathbf{R}}(E_i(\mathbf{R}) - E_j(\mathbf{R})) \quad (2)$$

where $\phi_i^a(\mathbf{x}; \mathbf{R})$ and $\phi_j^a(\mathbf{x}; \mathbf{R})$ are the adiabatic electronic states between which the system switches during the hop, \mathbf{R} is the vector of nuclear coordinates, \mathbf{x} is the vector of electronic coordinates, $\nabla_{\mathbf{R}}$ is the gradient with respect to nuclear coordinates, and $E_i(\mathbf{R})$ and $E_j(\mathbf{R})$ are the adiabatic energies of states $\phi_i^a(\mathbf{x}; \mathbf{R})$ and $\phi_j^a(\mathbf{x}; \mathbf{R})$ as functions of \mathbf{R} . The \mathbf{g} prescription (throughout this paper, we drop the subscripts and arguments of \mathbf{d} and \mathbf{g} where it will not cause confusion; i.e., \mathbf{g} denotes $\mathbf{g}_{12}(\mathbf{R})$ and \mathbf{d} denotes $\mathbf{d}_{12}(\mathbf{R})$) is computationally more convenient, but the \mathbf{d} prescription has been recommended by Tully⁵ and Stine and Muckerman,⁶ and it has been justified theoretically on the basis of semiclassical theory.^{7,8} However, recent work comparing the \mathbf{d} and \mathbf{g} hopping prescriptions for a variety of systems^{9,10} showed no notable difference in results between using the two methods. This was also reported earlier by Eaker.¹¹ We can explain this in part by the fact that it has been shown

[†] University of Minnesota.

[‡] NASA Ames Research Center.

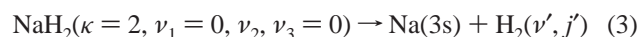
that the **d** and **g** vectors are parallel in systems with constant diabatic coupling.¹² Therefore, the **d** and **g** vectors are expected to give similar results in any system in which the diabatic coupling is approximately constant in the regions where most nonadiabatic transitions occur. This does not explain all the observed results, though, since it was also found⁴ that the final state distributions are almost independent of the choice of **d** versus **g** in a system where the **d** and **g** vectors are nearly perpendicular to each other. The **d** and **g** vectors are also expected to give similar results in any system with a small average potential energy gap at hopping events, since in this case the change in the kinetic energy is relatively small. A systematic study of the differences in the dynamics observed when using the **d** or **g** vector to adjust the momentum has never been reported.

In this work, we present calculations on the unimolecular decay of exciplexes. We use a realistic diabatic potential energy matrix (NaH₂ potential energy matrix 6)²¹ for which the diabatic coupling is not constant at most geometries. The **d** and **g** vectors generally point in different directions in this system, including the range of geometries where most surface hops occur. We present converged quantum dynamics calculations and TSH calculations carried out by Tully's fewest switches^{5,15,16} (TFS) method over a range of initial states and energies.

A problem that occurs in both momentum-adjusting prescriptions described above is the possibility that there may be insufficient momentum along the vector to allow a hop. This occurs only in transitions from a lower energy surface to a higher energy surface. Suggested remedies for this problem include simply ignoring the surface change¹³ or reversing the component of the momentum along the hopping vector (**d** or **g**),³ as if a step function in the potential surface had been encountered. In both cases, the trajectory remains on the same surface. In the TFS method, the undesirable consequence of either of these procedures is that the correct ensemble-averaged electronic populations are not maintained. This is because surface hops and associated electronic state switches are enforced to maintain the correct populations in an ensemble-averaged sense. The hops must occur where there is a local change in the probability of being on the current potential energy surface. Once the correct hopping position has been passed, there is no mechanism to allow a correction for inadequate tracking. Thus, in the TFS method, it is important that the correct populations always be maintained. In this paper, we examine the dynamical consequences of allowing the **d** or **g** vector to rotate in order to allow surface transitions to occur and to reduce the number of momentum-prohibited hops. The TFS calculations were performed with the **d** prescription (TFS-**d**) and the **g** prescription (TFS-**g**) and with two new prescriptions called rotated **d** and rotated **g**.

2. System

The process we consider is electronic predissociation, i.e., the unimolecular decay of an electronically excited-state complex to ground-electronic-state fragments, in particular,



where the left-hand side represents an exciplex, κ is the initial electronic state ($\kappa = 1$ is the electronic ground state, \tilde{X} , and $\kappa = 2$ is the first excited state, \tilde{A}), ν_l ($l = 1, 2$, or 3) are the quantum numbers for the H₂ stretch, the symmetric Na–H₂ stretch, and the asymmetric Na–H₂ bend, respectively, and ν' and j' are the final vibrational and rotational quantum numbers

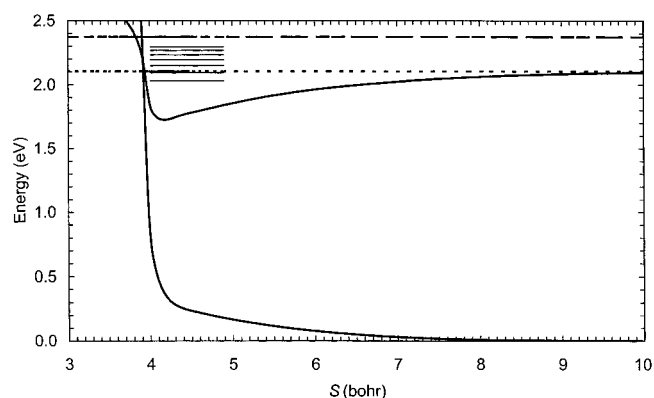


Figure 1. Schematic diagram of cuts through the potential energy surfaces of the first two diabatic states of the NaH₂ system as a function of S (distance from Na to H₂). For this figure, s (distance from H to H) was optimized for each value of S . The geometries shown have C_{2v} symmetry, for which the diabatic and adiabatic representations are identical and for which the diabatic coupling is zero. The electronic symmetry of the ground diabatic state, \tilde{X} , is A_1 , and the electronic symmetry of the first excited diabatic state, \tilde{A} , is B_2 . The long-dashed line at 2.373 eV represents the zero-point energy of H₂ + Na(3p). The short-dashed line represents the classical asymptotic Na(3p) + H₂ energy without zero-point energy. The short solid lines represent the energies of funnel resonances.

of H₂. We consider values of ν_2 in the range 0–6. Note that the \tilde{A} state corresponds formally to Na(3p) complexed to H₂, whereas the repulsive \tilde{X} state corresponds to Na(3s) + H₂. In this work, we neglect spin–orbit coupling and electronic angular momentum. We consider only states with zero total angular momentum. We use a two-state diabatic potential energy matrix (NaH₂ potential energy matrix 6)²¹ for all of the calculations. Analytical derivatives for this potential matrix were calculated using the ADIFOR²² PROGRAM.

A schematic diagram of the diagonal matrix elements at C_{2v} geometries is shown in Figure 1. In this figure and elsewhere, we use the following three Jacobi coordinates: S (distance from Na to H₂), s (distance from H to H), and χ (the angle between the Na-to-H₂ center and H₂ axis). Throughout this paper, the zero of energy corresponds to Na(3s) infinitely far from the H₂ diatom. The well in the excited state surface in Figure 1 is the exciplex, also called a funnel.^{23,24} In Figure 1, it can be seen that the crossing of the diabats occurs at energies slightly higher than the asymptotic Na(3p) + H₂ energy. Note that five of the energies occur above the asymptotic Na(3p) + H₂ energy and are not classically bound.

The vibrational quantum numbers of each of the three exciplex modes, listed together, are used as a shorthand notation throughout this paper. For example, 000 refers to the lowest energy exciplex state and 100 refers to the state which has one quanta of energy in the H₂ vibrational mode.

3. Quantum Mechanical Theory

We used accurate quantum mechanical scattering calculations to locate and characterize the predissociating states. These states show up in scattering calculations as electronic Feshbach resonances.²⁵ We will call them Feshbach funnel resonances.²⁶ The methods we used to locate and characterize these kinds of states were described in earlier work.^{26,27} We summarize the process here.

The eigenphase sum, $\Delta(E)$, is defined by

$$\exp(2i\Delta(E)) = \det \mathbf{S}(E) \quad (4)$$

where $\mathbf{S}(E)$ is the scattering matrix and E is the total energy at

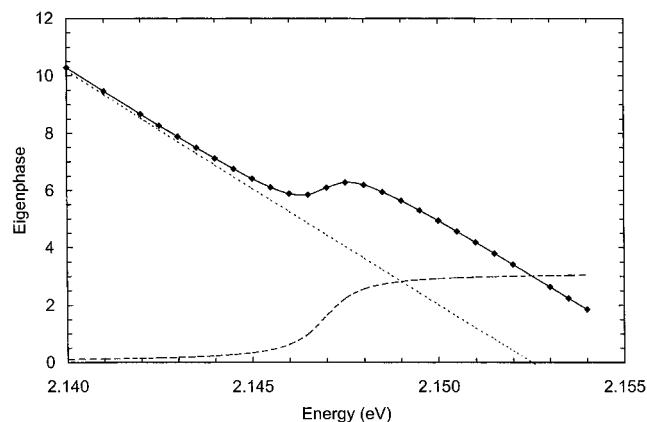


Figure 2. Smoothed eigenphase sums as functions of energy in the region of a resonance. The solid diamonds represent quantum mechanical eigenphase sums, smoothed by addition of multiples of π . The solid line represents the fit to these points. The dotted line represents the background contribution to the eigenphase sum, and the short dashed line represents the resonance contribution to the eigenphase sum.

which $S(E)$ and $\Delta(E)$ are calculated. This formula only determines $\Delta(E)$ to within a multiple of π . In order to obtain $\Delta(E)$ as a smooth function of energy, multiples of π were added where necessary for continuity. We use the notation $\Delta(E)$ to indicate eigenphase sums calculated from eq 4 and smoothed by addition of multiples of π .

According to the multichannel analogy of the Breit–Wigner formula, in the region of an isolated narrow resonance, the eigenphase sum is given approximately by²⁸

$$\Delta(E) = \Delta^b(E) + \arctan\left(\frac{\Gamma_\alpha}{2(E_\alpha - E)}\right) \quad (5)$$

where $\Delta^b(E)$ is the background contribution to the eigenphase sum, Γ_α is the total width of the resonance, E_α is the resonance energy, and the arctan is always chosen to be the branch between 0 and π (not $-\pi/2$ to $\pi/2$). Our goal is to fit eq 5 to the quantum mechanical $\Delta(E)$ values to determine Γ_α and E_α . We expand $\Delta^b(E)$ in a polynomial of the energy

$$\Delta^b(E) = \sum_{l=0}^P a_l E^l \quad (6)$$

where P is the order of the polynomial. We fit eq 5 with the substitution (6) to the accurate data $\Delta^{\text{acc}}(E_k)$ at N_E points E_k by minimizing the following quantity:²⁷

$$\delta^2 = \frac{1}{N_E - P - 2} \sum_{k=1}^{N_E} [\Delta^{\text{fit}}(E_k) - \Delta^{\text{acc}}(E_k)]^2 \quad (7)$$

Our general procedure was to select a value of P and to minimize eq 7 with respect to Γ_α , E_α , and a_l . We then increased P and repeated the process. We typically found that Γ_α and E_α were stable with respect to the variation of P in the region of the optimal value of P . Figure 2 shows a plot of $\Delta^{\text{fit}}(E_k)$, $\Delta^{\text{acc}}(E_k)$, and the background and resonance components of $\Delta^{\text{fit}}(E_k)$ versus E .

Once we had determined Γ_α and E_α , we calculated the partial widths according to the formula^{29–32}

$$S_{n'n}(E_k) = S_{n'n}^b(E_k) - i \frac{\gamma_{\alpha n'} \gamma_{\alpha n}}{E_k - z_\alpha} \quad (8)$$

where

$$z_\alpha = E_\alpha - i \frac{\Gamma_\alpha}{2} \quad (9)$$

and $S_{n'n}(E_k)$ is an approximation to $S_{n'n}$ (an element of $S(E)$), $S_{n'n}^b(E_k)$ is the background scattering contribution to $S_{n'n}(E_k)$, and $\gamma_{\alpha n}$ and $\gamma_{\alpha n'}$ are partial widths describing decay from the resonance α into the n and n' channels, respectively. $S_{n'n}^b(E_k)$ is expanded in a polynomial as a function of energy:

$$S_{n'n}^b(E_k) = \sum_{j=0}^{P'} A_{jn'n} E_k^j \quad (10)$$

where P' is the order of the polynomial. Multiplying by $E - z_\alpha$ gives

$$(E - z_\alpha) S_{n'n} = \sum_{j=0}^{P'+1} B_{jn'n} E^j \quad (11)$$

where

$$B_{P'+1,n'n} = A_{P'n'n} \quad (12)$$

$$B_{jn'n} = A_{n-1,n'n} - z_\alpha A_{jn'n} \quad j = 1, 2, \dots, P' \quad (13)$$

$$B_{0n'n} = -z_\alpha A_{0n'n} - i C_{\alpha n'n} \quad (14)$$

and

$$C_{\alpha n'n} = \gamma_{\alpha n'} \gamma_{\alpha n} \quad (15)$$

Note that all of the polynomial coefficients given above are complex.

The quantity $C_{\alpha n'n}$ is determined by fitting eq 8 to an entire column of the S matrix by minimizing the following quantity:

$$\epsilon_n^2 = \sum_{n'=1}^{N_c} \left[\frac{\sum_k |S_{nn'} - S_{nn'}(E_k)|^2}{N_E - P'} \right]^{1/2} \quad (16)$$

where the summation is over all of the open channels, N_c . Once $C_{\alpha n'n}$ is determined, $\gamma_{\alpha n'}$ and $\gamma_{\alpha n}$ are calculated from

$$\gamma_{\alpha n'} = \frac{C_{\alpha n'n}}{\sqrt{C_{\alpha nn}}} \quad (17)$$

In practice, we fit all n columns of the $S(E)$ matrix, and we report data from the column that had the largest partial width. A more detailed description of the procedure for fitting partial widths is given in earlier work.^{26,27}

We define the probability of decay of resonance α into channel n as

$$P_{\alpha n} = \frac{|\gamma_{\alpha n}|^2}{G_\alpha} \quad (18)$$

where

$$G_\alpha = \sum_{n=1}^{N_c} |\gamma_{\alpha n}|^2 \quad (19)$$

G_α equals Γ_α for an isolated narrow resonance, but for the resonances, we consider that G_α tends to be slightly smaller than Γ_α .

The final average vibrational and rotational quantum numbers for the decay products of each exciplex are given in terms of the decay probabilities as follows:

$$\langle \nu' \rangle_\alpha = \sum_n P_{\alpha n} \nu'_n \quad (20)$$

$$\langle j' \rangle_\alpha = \sum_n P_{\alpha n} j'_n \quad (21)$$

where the summation is over all open channels and ν'_n and j'_n are the vibrational and rotational quantum numbers of channel n , respectively. The subscript α on $\langle \nu' \rangle$ and on $\langle j' \rangle$ labels the resonance.

The mean lifetime for a resonance is given by^{31–34}

$$\tau_\alpha = \frac{\hbar}{\Gamma_\alpha} \quad (22)$$

where the subscript α again labels the resonance.

4. Computational Methods

4.1. Quantum Mechanical Scattering. The accurate quantum mechanical calculations were carried out by the hybrid basis set outgoing wave variational principle (OWVP)^{35,36} using version 18.5 of the vp computer code.³⁷ Table 1 lists the basis set parameters for two different basis sets. These parameters are described in full detail in an earlier paper,³⁶ and we give a brief summary of these parameters in Table 2. Basis set I was used for all of our OWVP calculations. Basis set II is a larger basis set, and it was used to check the level of convergence of basis set I. We performed calculations at a range of energies with both basis sets, and we compared the state-to-state transition probabilities at each energy. A summary of the convergence is shown in Figure 3. Shown are the number of transition probabilities in each range of magnitude and the relative convergence for that group. At 2.030 eV, the transition probabilities larger than 1×10^{-6} are all converged to within 1–2%. At 2.232 eV, the basis set is slightly less well-converged. Most of the transition probabilities larger than 1×10^{-5} are converged to within 2–5%, and about half of them are converged to within 1%. Note that the energies shown in Figure 3 correspond to the locations of resonances. It is difficult to converge the quantum calculations with respect to the basis set size and with respect to numerical parameters at these energies because of the notorious sensitivity of scattering calculations to all parameters near a resonance. Calculations at energies that do not correspond to the location of resonances are converged to an even higher degree.

We checked the convergence of $\langle \nu' \rangle$ and $\langle j' \rangle$ by performing a series of calculations in the neighborhood of the resonance at 2.232 eV with basis set II and comparing these results to calculations obtained with basis set I. Table 3 illustrates the differences between these calculations, and it illustrates the effect of using different parameters for the fit of the partial widths described in section 3. It can be seen that the average final vibrational and rotational quantum numbers are stable with respect to a change in these parameters and that they are converged with respect to the basis set.

We need eigenphase sums over a range of energies in order to locate resonances by the method described in section 3. The spacing of the energies needs to be about a half of the width of

TABLE 1: Basis Set Parameters for OWVP Calculations

parameter	basis set	
	I	II
$j_{\max}(\kappa = 1, \nu = 0)$	24	26
$j_{\max}(\kappa = 1, \nu = 1)$	22	24
$j_{\max}(\kappa = 1, \nu = 2)$	20	22
$j_{\max}(\kappa = 1, \nu = 3)$	17	19
$j_{\max}(\kappa = 1, \nu = 4)$	15	17
$j_{\max}(\kappa = 1, \nu = 5)$	12	14
$j_{\max}(\kappa = 1, \nu = 6)$	8	10
$j_{\max}(\kappa = 1, \nu = 7)$	2	4
$j_{\max}(\kappa = 1, \nu = 8)$		4
$j_{\max}(\kappa = 2, \nu = 0)$	18	20
$j_{\max}(\kappa = 2, \nu = 1)$		16
$\nu_{\max}^a(\kappa = 1)$		7
$j_{\max}^{\text{vib}}(\kappa = 1)$		21
$\nu_{\max}^a(\kappa = 2)$	10	11
$j_{\max}^{\text{vib}}(\kappa = 2)$	22	24
$\Delta^{\text{vib}}(\kappa = 1)$		0.18
$\Delta^{\text{vib}}(\kappa = 2)$	0.16	0.16
$w^{\text{vib}}(\kappa = 1)$		0.3
$w^{\text{vib}}(\kappa = 2)$	0.3	0.33
$\Delta^S(\kappa = 1, \text{all } \nu)$	0.120	0.120
$\Delta^S(\kappa = 2, \text{all } \nu)$	0.132	0.132
$\Delta^S(\kappa = 2, \text{all } \nu^a)$	0.132	0.132
$\Delta^S(\kappa = 1, \text{all } \nu^a)$		0.217
$c(\kappa = 1, \text{all } \nu)$	0.48	0.44
$c(\kappa = 1, \text{all } \nu^a)$		0.96131
$c(\kappa = 2)$	0.74	0.70
$s_1^{\text{vib}}(\kappa = 1)$		2.46
$s_u^{\text{vib}}(\kappa = 1)$		3.54
$s_1^{\text{vib}}(\kappa = 2)$	1.040	0.960
$s_u^{\text{vib}}(\kappa = 2)$	2.480	2.560
$S_1^G(\kappa = 1, \text{all } \nu)$	2.816	2.756
$S_u^G(\kappa = 1, \text{all } \nu)$	8.936	8.996
$S_1^G(\kappa = 1, \text{all } \nu^a)$		2.888
$S_u^G(\kappa = 1, \text{all } \nu^a)$		5.709
$S_1^G(\kappa = 2, \text{all } \nu)$	2.312	2.246
$S_u^G(\kappa = 2, \text{all } \nu)$	9.44	9.506
$S_1^G(\kappa = 2, \text{all } \nu^a)$	2.312	2.246
$S_u^G(\kappa = 2, \text{all } \nu^a)$	10.76	10.826
$m_1^g, m_1^c(\text{all } \nu)$	52	53
$m_1^a(\text{all } \nu^a)$		14
$m_2^g, m_2^c(\text{all } \nu)$	55	56
$m_2^a(j \leq 9, \nu^a)$	65 (1–7)	66 (1–8)
$m_2^a(j \leq 9, \nu)$	55 (8–10)	56 (9–11)
$m_2^a(j > 9, \nu^a)$	55 (1–10)	56 (1–11)
ϵ_k	12	14
ϵ_t	100	100
ϵ_{rad}	14	16
$\epsilon_{\mathcal{B}}$	12	14
ϵ_W	12	14
$N(\text{HO})$	80	90
N^{QGLV}	80	80
N^{QV}	720	800
N^{QA}	150	200
s_1^{QV}	0	0
s_u^{QV}	5.0	5.5
N^{FD}	15	15
$N(\text{F})$	1825	2140
S_0^F	1.0	0.8
S_0^{QV}	40.0	45.0
$N^{\text{QGL}}_{N(\text{F})+1}$	7	7
N^{QS}	255	300
N^{SD}	40	40
f^{SD}	0.9	0.9
S_1^{QR}	1.0	0.8
S_u^{QR}	30.0	35.0

TABLE 2: Description of Scattering Basis Set Parameters Used in Table 1

parameter	description
$j_{\max}(\kappa, \nu)$	max rotational quantum number for this κ, ν
$\nu_{\max}^a(\kappa)$	max number of vibrational distributed Gaussians for this κ
$j_{\max}^{\text{vib}}(\kappa)$	max rotational level associated with each vibrational distributed Gaussian for this κ
$\Delta^{\text{vib}}(\kappa)$	spacing of the vibrational distributed Gaussians in unscaled coordinates for this κ
$w^{\text{vib}}(\kappa)$	width parameter for the vibrational distributed Gaussians for this κ
$\Delta^S(\kappa, \nu)$	spacing of the translational distributed Gaussians for this κ, ν (or ν^a)
$c(\kappa, \nu)$	overlap parameter for the translational distributed Gaussians for this κ, ν (or ν^a)
$s_1^{\text{vib}}(\kappa)$	center of the first vibrational distributed Gaussian, for this κ
$s_u^{\text{vib}}(\kappa)$	center of the last vibrational distributed Gaussian, for this κ
$s_1^G(\kappa, \nu)$	center of the first translational distributed Gaussian, for this κ, ν (or ν^a)
$s_u^G(\kappa, \nu)$	center of the last translational distributed Gaussian, for this κ, ν (or ν^a)
$m_k^x(\nu, j)$	total number of translational distributed Gaussians per ν, j (or ν^a, j) channel assigned to surface κ , basis function type x ($x = g$ (half-integrated Green's function), e (asymptotic eigenstate function), or a (vibrationally distributed Gaussian functions))
ϵ_k	vibrational screening parameter
ϵ_t	translational screening parameter
ϵ_{rad}	radial screening parameter
ϵ_B	screening parameter involving the B matrix
ϵ_W	screening parameter involving the W matrix
$N(\text{HO})$	number of harmonic oscillator basis functions used to expand the diatomic adiabatic vibrational eigenfunctions
N^{QLV}	number of quadrature points per repetition used in the Gauss–Legendre quadrature over the vibrational coordinate
N^{QV}	total number of quadrature points used in the Gauss–Legendre quadrature over the vibrational coordinate
N^{QA}	number of points in the Gauss–Legendre quadrature used for angular integrals
s_1^{QV}	lower limit on the vibrational quadrature grid
s_u^{QV}	upper limit on the vibrational quadrature grid
N^{FD}	number of points used in the finite difference representation of the second-derivative operator
$N(F)$	number of finite difference grid points
S_0^F	small- S finite difference boundary condition point
S_0^{QV}	large- S finite difference boundary condition point
$N_{\text{QGL}}^{N(F)+1}$	number of radial quadrature points per repetition of Gauss–Legendre quadrature
N^{QS}	number of repetitions of Gauss–Legendre quadrature over the radial coordinate
N^{SD}	number of additional points at the end of the finite difference grid where step size decrease occurs
f^{SD}	step size decrease factor
S_1^{QR}	lower limit on the quadratures over the radial variable S
S_u^{QR}	upper limit on the quadratures over the radial variable S

the resonance (or smaller) in order for the resonance to appear on a plot of the eigenphase sums. The region over which resonances might be expected to occur can be calculated from the difference in energy between the Na(3p) + H₂(0,0) channel and the NaH₂ 000 state. Since the zero-point energy of the NaH₂ exciplex is roughly equal to the zero-point energy of H₂, the energy range over which we need calculations is approximately equal to the depth of the exciplex well relative to the Na(3p) + H₂ asymptote, which is about 0.4 eV. It would therefore require calculations at about 800 energies to search this entire range for resonances whose widths are about 1 meV.

In order to reduce the number of calculations required for the search, we tried two different methods to predict the location of resonances before carrying out the scattering calculations. First, we attempted to estimate the location of the resonances by making the separable-mode approximation and solving three independent one-dimensional problems. We calculated one-dimensional slices of the potential energy surface at the bottom of the exciplex along the three Jacobi coordinates. We then fit these slices to one-dimensional Morse curves, and we solved for the quantum energy levels.

Unfortunately, the uncoupled procedure was not accurate enough to predict the resonance energies. As can be seen by examining Figure 2, resonances are essentially invisible at energies that differ by as little as 10 meV from the center of the resonance, and the predictions given by the separable approximation are larger than this.

The second procedure we used proved to be much more effective. This procedure consisted of performing variational bound-state calculations on the uncoupled upper adiabatic energy surface. These calculations included all potential energy coupling

between the nuclear coordinates, they used the Jacobi coordinates for Na + H₂, and they used the exact kinetic energy operator. The program used is described elsewhere.³⁸ The calculations are straightforward, except that difficulties were encountered when evaluating the radial integrals over the potential because the potential is not sufficiently smooth. Thus, rather than using a single Gaussian-like quadrature to evaluate the radial integrals, the integration region was divided into 10 intervals, each having its own quadrature.³⁹ In order to improve the convergence of the energy levels with high Na + H₂ stretching quantum numbers, we enclosed the potential in a soft box by adding a steep repulsive potential starting at 9 a₀.³⁹ Figures 4–6 show plots of the wave-function density for the 000, the 010, and the 020 states of the single-surface calculations. Note the trend of the density extends to larger S distances with higher vibrational excitation.

We found a resonance with the OWVP calculations to correspond to each resonance predicted by the bound-state calculations. A comparison of the OWVP-calculated energies of each resonance with the bound-state predictions is given in Table 4. We made the state assignments as follows. The 000 state must correspond to the resonance in the even-symmetry calculations at the lowest energy, which was 2.030 eV. The resonance at 2.184 eV was the lowest energy resonance in the odd-symmetry calculations. Therefore, this resonance corresponds to the 001 state. The resonance at 2.093 eV could correspond to the excitation of either the H₂ stretch or the Na–H₂ stretch. Since the H₂ stretch has a higher frequency, we assign the 010 state to the resonance at 2.093 eV. The resonances at 2.147, 2.193, 2.232, 2.267, and 2.296 eV show energy spacings consistent with progressive $0n0$ excitation. We also note a

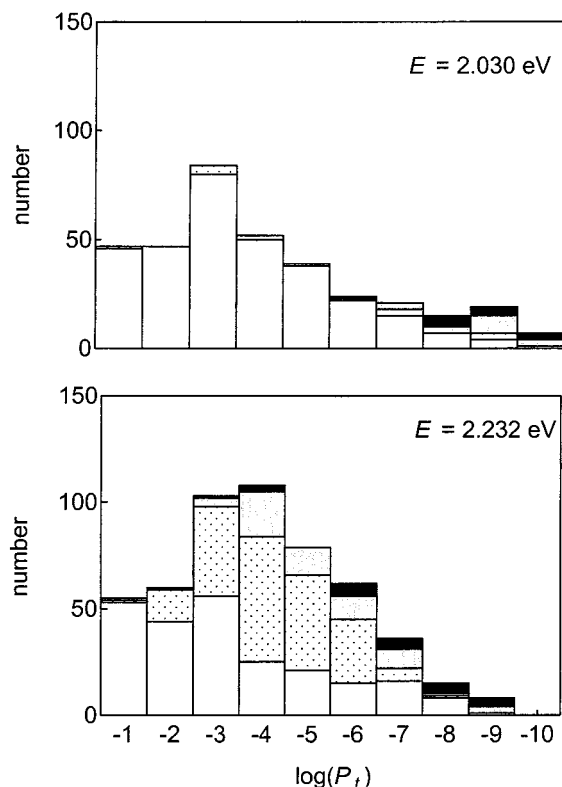


Figure 3. Number of transition probabilities that fell into each range of magnitude. The shading indicates the degree of convergence: white indicates convergence to 1%, black dots indicate convergence to 2%, gray indicates convergence to 5%, and solid black indicates convergence worse than 5%.

progressive change in the lifetimes and final average quantum numbers for these resonances. We therefore assigned the 020–060 states to them.

The resonance at 2.273 eV could correspond to either the 100 state or the 002 state. The largest coefficient of the bound-state basis functions at this energy is only 0.532, and therefore, making an assignment based on the character of the bound-state wave function is difficult. The dynamical information from the OWVP calculations is more suggestive. The total width for this state is small, and it is similar in size to the width of the resonance corresponding to the 001 state. Classically, we might think of the bending motion as moving the system away from the C_{2v} geometries where the conical intersection occurs and, therefore, prolonging its life. Quantum mechanically, we expect the wave function to have a significant part of its density at non- C_{2v} geometries. We assigned the 002 state to the resonance at 2.273 eV for this reason. We expect the resonance corresponding to the 100 state to have a much shorter lifetime, since motion along the H_2 vibrational coordinate would tend to bring the system across the conical intersection. The resonance at 2.302 eV is a good candidate by this criteria. Also, the final vibrational moment of the decay products of the resonance at 2.302 eV is larger than the vibrational moments of the other resonances' decay products. This is consistent with the idea that the wave function describing a semibound state with H_2 vibrational excitation will have a large overlap with ground-state basis functions that have high vibrational quantum numbers. On the basis of these dynamical considerations, we assigned the 100 state to the resonance at 2.302 eV.

We note that the difference between the OWVP calculations of E_α and the bound-state calculations of E_α is the "shift" of Feshbach theory.⁴⁰

TABLE 3: Convergence of the Decay Probabilities and Final Average Rotational and Vibrational Quantum Numbers for the Resonance at 2.232 eV

row	ν'	j'	standard ^a	$O(P) = 5$	column 9	basis set II
1	0	0	6.39×10^{-4}	6.34×10^{-4}	6.39×10^{-4}	6.40×10^{-4}
2	0	2	3.12×10^{-3}	3.09×10^{-3}	3.12×10^{-3}	3.12×10^{-3}
3	0	4	6.31×10^{-3}	6.35×10^{-3}	6.31×10^{-3}	6.32×10^{-3}
4	0	6	2.17×10^{-2}	2.17×10^{-2}	2.17×10^{-2}	2.17×10^{-2}
5	0	8	7.21×10^{-2}	7.19×10^{-2}	7.21×10^{-2}	7.22×10^{-2}
6	1	0	4.75×10^{-4}	4.84×10^{-4}	4.75×10^{-4}	4.70×10^{-4}
7	1	2	2.85×10^{-2}	2.85×10^{-2}	2.85×10^{-2}	2.85×10^{-2}
8	1	4	1.59×10^{-2}	1.61×10^{-2}	1.59×10^{-2}	1.59×10^{-2}
9	0	10	1.49×10^{-1}	1.47×10^{-1}	1.49×10^{-1}	1.49×10^{-1}
10	1	6	2.43×10^{-2}	2.43×10^{-2}	2.43×10^{-2}	2.44×10^{-2}
11	1	8	2.20×10^{-3}	2.24×10^{-3}	2.20×10^{-3}	2.23×10^{-3}
12	2	0	3.80×10^{-1}	3.83×10^{-1}	3.80×10^{-1}	3.80×10^{-1}
13	0	12	6.12×10^{-3}	6.28×10^{-3}	6.12×10^{-3}	6.13×10^{-3}
14	2	2	1.22×10^{-1}	1.20×10^{-1}	1.22×10^{-1}	1.22×10^{-1}
15	2	4	1.29×10^{-2}	1.33×10^{-2}	1.29×10^{-2}	1.29×10^{-2}
16	1	10	7.44×10^{-4}	7.42×10^{-4}	7.44×10^{-4}	7.25×10^{-4}
17	2	6	6.72×10^{-4}	6.60×10^{-4}	6.71×10^{-4}	6.57×10^{-4}
18	0	14	3.13×10^{-2}	3.07×10^{-2}	3.13×10^{-2}	3.12×10^{-2}
19	2	8	1.47×10^{-3}	1.47×10^{-3}	1.47×10^{-3}	1.48×10^{-3}
20	3	0	1.62×10^{-2}	1.67×10^{-2}	1.62×10^{-2}	1.56×10^{-2}
21	1	12	9.53×10^{-3}	9.62×10^{-3}	9.53×10^{-3}	9.54×10^{-3}
22	3	2	3.96×10^{-3}	4.07×10^{-3}	3.96×10^{-3}	3.84×10^{-3}
23	3	4	1.11×10^{-4}	1.10×10^{-4}	1.11×10^{-4}	1.07×10^{-4}
24	0	16	7.33×10^{-2}	7.48×10^{-2}	7.33×10^{-2}	7.36×10^{-2}
25	2	10	1.79×10^{-3}	1.83×10^{-3}	1.79×10^{-3}	1.79×10^{-3}
26	3	6	3.63×10^{-4}	3.64×10^{-4}	3.63×10^{-4}	3.62×10^{-4}
27	1	14	1.36×10^{-2}	1.34×10^{-2}	1.36×10^{-2}	1.37×10^{-2}
28	3	8	1.54×10^{-4}	1.56×10^{-4}	1.54×10^{-4}	1.54×10^{-4}
29	4	0	1.53×10^{-3}	1.57×10^{-3}	1.53×10^{-3}	1.54×10^{-3}
30	2	12	2.21×10^{-5}	2.23×10^{-5}	2.21×10^{-5}	2.20×10^{-5}
31	4	2	2.67×10^{-6}	2.75×10^{-6}	2.67×10^{-6}	2.63×10^{-6}
$\langle \nu' \rangle$			1.202	1.205	1.202	1.200
$\langle j' \rangle$			4.849	4.840	4.849	4.857

^a A fourth-order polynomial fit to the column of the S matrix with the largest partial width (column 12). Basis set I was used in the S matrix calculation. Each of the other columns deviate from the standard method in the order of the polynomial ($O(P)$), the column used in the fit, or the basis set used in the calculation of the S matrix.

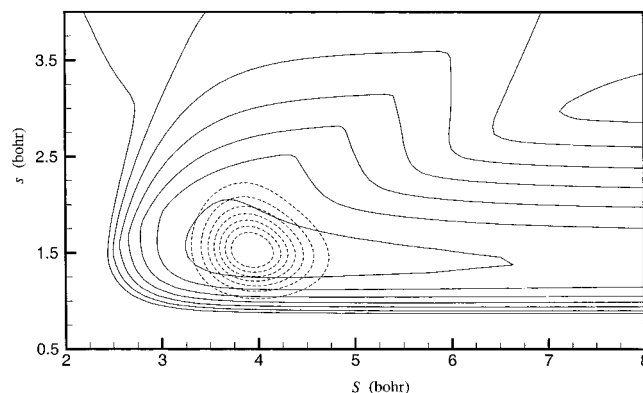


Figure 4. Plot of the wave-function density of the 000 bound state on the excited adiabatic potential surface. The potential energy contours (solid lines) are shown for 2.0, 2.5, ..., 5.0 eV. The dashed contours represent the wave-function density.

4.2. Trajectory Surface Hopping. All trajectories are carried out in the adiabatic representation.

4.2.1. Selection of the Initial Conditions. The initial conditions for the trajectory calculations were chosen to correspond to particular resonance states located by our OWVP calculations. We assigned quasiclassical energies to each mode according to the following scheme:

$$E_{\nu_1} = f_1 E_{\text{ZPE}} \quad (23)$$

$$E_{v_2} = f_2 E_{\text{ZPE}} + E(0, v_2, 0) - E(0, 0, 0) \quad (24)$$

$$E_{v_3} = f_3 E_{\text{ZPE}} \quad (25)$$

$$f_1 = \frac{E(1, 0, 0) - E(0, 0, 0)}{E(1, 0, 0) + E(0, 1, 0) + E(0, 0, 1) - 3E(0, 0, 0)} \quad (26)$$

$$f_2 = \frac{E(0, 1, 0) - E(0, 0, 0)}{E(1, 0, 0) + E(0, 1, 0) + E(0, 0, 1) - 3E(0, 0, 0)} \quad (27)$$

$$f_3 = \frac{E(0, 0, 3) - E(0, 0, 0)}{E(1, 0, 0) + E(0, 1, 0) + E(0, 0, 1) - 3E(0, 0, 0)} \quad (28)$$

$$f_1 + f_2 + f_3 = 1 \quad (29)$$

where E_{ZPE} is the quantal zero-point energy, $E(v_1, v_2, v_3)$ is the quantal energy of the $v_1 v_2 v_3$ state, and E_{v_l} is the quasiclassical energy in mode l . Note that the quantal energies are already calculated from OWVP calculations by the method of section 3. The quantities $f_l E_{\text{ZPE}}$ ($l = 1, 2$, or 3) are a partition of the zero-point energy into each mode according to the size of the first excitation energy of that mode. Note that this partitioning is somewhat arbitrary and other partitioning methods could be considered; however, we chose this method because it does not depend on any assumptions about the potential (e.g., that it is well approximated by a Morse curve), but it is still formally correct in the ideal case of three totally independent harmonic oscillators.

Once we had partitioned the total energy into each of the three vibrational modes, we partitioned each modal energy into potential energy and kinetic energy components by randomly selecting the vibrational phase of each mode. Since the three vibrational modes are not exactly separable, this prescription resulted in trajectories with a distribution of total energies. In order to make the energy of each trajectory equal to $E(v_1, v_2, v_3)$, we scaled the momentum along each mode by a factor $[E(v_1, v_2, v_3) - V]/(E_{v_l} - V)^{1/2}$, where V is the potential energy. In cases where V was greater than $E(v_1, v_2, v_3)$, we set the momentum to zero and we adjusted the coordinates along the negative gradient of V by the smallest amount necessary to make the energy of the trajectory equal to $E(v_1, v_2, v_3)$.

4.2.2. TFS Methods. It is convenient to label the Na atom as A and the H atoms as B and C. Integration is carried out in a six-dimensional coordinate space consisting of the three-vector \mathbf{S} from A to the center of mass of BC and the three-vector \mathbf{s} from B to C. It is convenient to carry out part of the calculations in mass-weighted coordinates defined by

$$\mathbf{Q} = \sqrt{u_{\text{A,BC}}} \mathbf{S} \quad (30)$$

$$\mathbf{q} = \sqrt{u_{\text{BC}}} \mathbf{s} \quad (31)$$

$$\mathbf{p}_Q = \mathbf{p}_S / \sqrt{u_{\text{A,BC}}} \quad (32)$$

$$\mathbf{p}_q = \mathbf{p}_s / \sqrt{u_{\text{BC}}} \quad (33)$$

where

$$\mu_{\text{A,BC}} = \frac{m_{\text{A}}(m_{\text{B}} + m_{\text{C}})}{m_{\text{A}} + m_{\text{B}} + m_{\text{C}}} \quad (34)$$

$$\mu_{\text{BC}} = \frac{m_{\text{B}} m_{\text{C}}}{m_{\text{B}} + m_{\text{C}}} \quad (35)$$

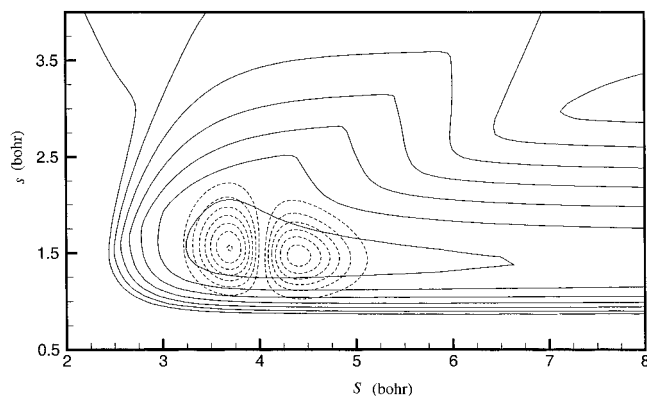


Figure 5. Plot of the wave-function density of the 010 bound state on the excited adiabatic potential surface. Contours are the same as for Figure 4.

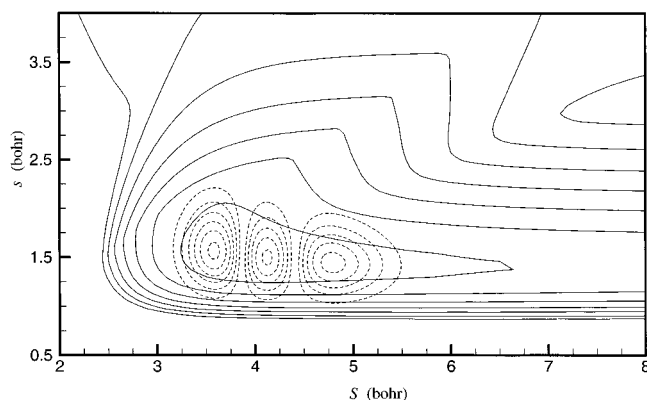


Figure 6. Plot of the wave-function density of the 020 bound state on the excited adiabatic potential surface. Contours are the same as for Figure 4.

m_X is the mass of atom X, and the momenta \mathbf{p}_Y are conjugate to the coordinates \mathbf{Y} . Note that the vectors \mathbf{q} , \mathbf{Q} , \mathbf{s} , \mathbf{S} , \mathbf{p}_q , \mathbf{p}_Q , \mathbf{p}_s , and \mathbf{p}_S are all in three-dimensional space.

For some purposes, it is useful to combine the three-vectors into six-vectors. For example, we define

$$\mathbf{R} = \begin{pmatrix} \mathbf{q} \\ \mathbf{Q} \end{pmatrix} \quad (36)$$

$$\mathbf{p}_R = \begin{pmatrix} \mathbf{p}_q \\ \mathbf{p}_Q \end{pmatrix} \quad (37)$$

Note that we have defined the nonadiabatic coupling vector $\mathbf{d}_{ij}(\mathbf{R})$ in eq 1 and the gradient in eq 2 as six vectors in the same mass-scaled coordinate space as \mathbf{R} .

We define a general unit vector $\hat{\mathbf{h}}$, which is a six-vector, along which the momentum (\mathbf{p}_R) of the trajectory is adjusted when hopping to conserve the total energy. We performed TFS calculations with four prescriptions for choosing this direction. Each prescription corresponds to a different version of the TFS method. Two of the vectors we used to adjust the momentum are the previously discussed \mathbf{d} and \mathbf{g} vectors. The calculation of \mathbf{d} and \mathbf{g} is summarized in Appendix A. The two new vectors are the rotated- \mathbf{d} (rot- \mathbf{d}) and rotated- \mathbf{g} (rot- \mathbf{g}) vectors, which we describe next.

In the remainder of this discussion, we examine methods for employing rotated vectors for surface hops from a lower energy surface to a higher energy surface (i.e., up hops), which are the only kinds of hops that can suffer from insufficient total energy

TABLE 4: Comparison of Bound-State Calculations and OWVP Calculations

α^a	$E_\alpha,^b$ eV	$\Gamma_\alpha,^b$ meV	OWVP						adiabatic bound state	
			v_1^c	v_2^c	v_3^c	$E_\alpha - E_0$ eV	$\langle v' \rangle$	$\langle j' \rangle$	$E_\alpha,^b$ eV	$E_\alpha - E_0,^b$ eV
0	2.030	1.442	0	0	0	0.000	0.82	8.34	2.030	0.000
1	2.093	1.279	0	1	0	0.063	0.74	7.69	2.094	0.064
2	2.147	1.385	0	2	0	0.117	0.84	7.25	2.148	0.118
3	2.184	0.608	0	0	1	0.154	1.85	5.67	2.184	0.154
4	2.193	1.222	0	3	0	0.163	1.09	5.67	2.194	0.164
5	2.232	1.116	0	4	0	0.202	1.20	4.85	2.233	0.203
6	2.267	1.020	0	5	0	0.237	1.30	4.32	2.268	0.238
7	2.273	0.522	0	0	2	0.243	1.35	8.82	2.273	0.243
8	2.296	0.848	0	6	0	0.266	1.34	3.73	2.297	0.267
9	2.302	2.871	1	0	0	0.272	2.41	2.98	2.304	0.274

^a Resonance. ^b Energy of resonance. ^c Exciplex vibrational modes.

or insufficient momentum along the hopping vector. Initially, $\hat{\mathbf{h}}$ points along either \mathbf{d} or \mathbf{g} , and we label this initial vector $\hat{\mathbf{h}}_0$. The amount of kinetic energy associated with the momentum along $\hat{\mathbf{h}}_0$ is given by

$$T_{\text{hop}}^0 = \frac{1}{2} (\mathbf{p}_R \cdot \hat{\mathbf{h}}_0)^2 \quad (38)$$

We note that mass does not appear in eq 38 since we are using mass-weighted momenta and mass-weighted coordinates. Appendix B shows how to decompose \mathbf{p}_R into a component \mathbf{p}_{vib} associated with the internal vibrational momentum and a component \mathbf{p}_{rot} associated with the external rotational momentum. By using that decomposition, we rewrite eq 38 as

$$T_{\text{hop}}^0 = \frac{1}{2} (\mathbf{p}_{\text{vib}} \cdot \hat{\mathbf{h}}_0 + \mathbf{p}_{\text{rot}} \cdot \hat{\mathbf{h}}_0)^2 \quad (39)$$

which reduces to

$$T_{\text{hop}}^0 = \frac{1}{2} (\mathbf{p}_{\text{vib}} \cdot \hat{\mathbf{h}}_0)^2 \quad (40)$$

since $\hat{\mathbf{h}}_0$ depends only on the internal coordinates of the system. We define θ_0 as the angle between $\hat{\mathbf{h}}_0$ and \mathbf{p}_{vib} and substitute it into eq 40, giving

$$T_{\text{hop}}^0 = \frac{1}{2} p_{\text{vib}}^2 \cos^2 \theta_0 \quad (41)$$

Equation 41 is an expression for the kinetic energy that is available for a surface hop as a function of the angle between the initial hopping vector and the internal vibrational momentum. Equation 41 indicates that the largest amount of kinetic energy available for a surface hop is

$$T_{\text{hop}}^{\text{max}} = \frac{1}{2} p_{\text{vib}}^2 \quad (42)$$

and that this maximum energy will only be available when the vibrational momentum is parallel to the hopping vector.

We define the adiabatic energy gap (E_{gap}) by

$$E_{\text{gap}}(\mathbf{R}) = E_2(\mathbf{R}) - E_1(\mathbf{R}) \quad (43)$$

and we note that the total kinetic energy is given by

$$T = \frac{1}{2} p_R^2 \quad (44)$$

We can then distinguish four possible situations in which up hops may be attempted:

$$\text{I: } E_{\text{gap}}(\mathbf{R}) \leq T_{\text{hop}}^0 \quad (45)$$

$$\text{II: } T_{\text{hop}}^0 < E_{\text{gap}}(\mathbf{R}) \leq T_{\text{hop}}^{\text{max}} \quad (46)$$

$$\text{III: } T_{\text{hop}}^{\text{max}} < E_{\text{gap}}(\mathbf{R}) \leq T \quad (47)$$

$$\text{IV: } T < E_{\text{gap}}(\mathbf{R}) \quad (48)$$

Case I corresponds to an allowed hop, case II to a momentum-forbidden hop, case III to an angular-momentum-forbidden hop, and case IV to an energy-forbidden hop. The rotated-vector method is concerned only with case II. In the rotated-vector method, we generalize eq 41 by allowing the hopping vector to be perturbed by an angle θ_{rot} so that the available kinetic energy is equal to the energy gap

$$\Delta E_{\text{gap}} = \frac{1}{2} p_{\text{vib}}^2 \cos^2(\theta_0 - \theta_{\text{rot}}) \quad (49)$$

It can be shown that this perturbed (rotated) vector is given in terms of $\hat{\mathbf{h}}_0$ and $\hat{\mathbf{p}}_{\text{vib}}$ by

$$\hat{\mathbf{h}} = \frac{\sin(\theta_0 - \theta_{\text{rot}})}{\sin \theta_0} \hat{\mathbf{h}}_0 + \frac{\sin \theta_{\text{rot}}}{\sin \theta_0} \hat{\mathbf{p}}_{\text{vib}} \quad (50)$$

A value of θ_{rot} equal to zero describes a vector identical to $\hat{\mathbf{h}}_0$, while a value of θ_{rot} equal to θ_0 describes a vector parallel to \mathbf{p}_{vib} . Note that θ_{rot} can be negative; a value of θ_{rot} equal to $\theta_0 - \pi$ describes a vector that points in the direction of $-\mathbf{p}_{\text{vib}}$. We choose the smallest absolute value of θ_{rot} that satisfies eq 49. Note that changing the momentum along the vector $\hat{\mathbf{h}}$ conserves the total angular momentum, since \mathbf{p}_{vib} and the momentum along $\hat{\mathbf{h}}_0$ have no angular momentum components. If, however, eqs 49 and 50 were derived with $\hat{\mathbf{p}}_R$ instead of with $\hat{\mathbf{p}}_{\text{vib}}$, then the resulting rotated hopping vector would have a component along $\hat{\mathbf{p}}_{\text{rot}}$, and changing the momentum along this rotated hopping vector would not conserve the total angular momentum.

4.2.3. Integration Scheme. Each integration step requires the integration of 21 coupled equations. These include the set of 12 Hamilton equations of motion for a 3-body system in Jacobi coordinates, the real and imaginary parts of the probability amplitudes for both potential energy surfaces, the action integral of each surface, and 3 more equations that required our implementation of the TFS method; these last 3 equations are discussed below.

The probability of a surface hop was calculated after each integration step. The calculation of the hopping probabilities will be discussed later in this section. If this probability was greater than a random number chosen in the interval [0,1], we checked to see whether we were in case I, II, III, or IV of the

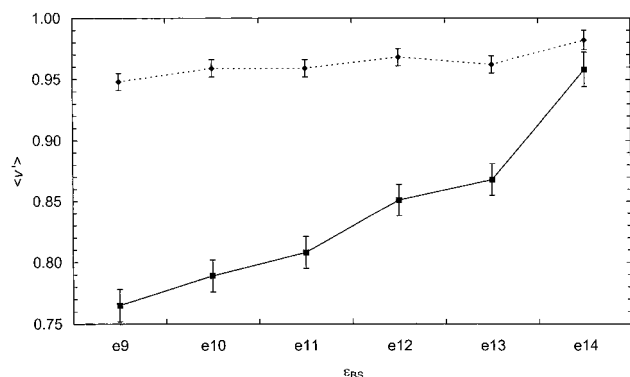


Figure 7. Final average vibrational quantum number versus the integrator tolerance ϵ_{BS} . The squares linked by solid lines represent calculations with the standard integration method, called method I. The diamonds linked by dashed lines represent calculations with a modified integration scheme called method II. Both methods are discussed in section 4.2.3. The error bars indicate 1 standard deviation.

previous section. If we were in case I, then a hop occurred and the kinetic energy was adjusted along the hopping vector \hat{h}_0 . If we were in case II and the rot-**d** or the rot-**g** prescription was being used, then a hop occurred and the kinetic energy was adjusted along \hat{h} . If we were in case II and the **d** or the **g** prescription was being used, then no hop occurred and the component of momentum along \hat{h}_0 was reversed. If we were in case III or in case IV, a hop did not occur. In case III, the momentum along \hat{h}_0 was reversed, while in case IV no change to the momentum was made. Our motivation for treating trajectories that attempt linear and angular momentum prohibited hops differently from trajectories that attempt energy-prohibited hops is that the former may be thought of as reflecting off a step in the potential surface that they encounter as they hop up,^{3,10} while the latter lack the energy to make a transition. After a successful hop, we took an additional integration step before again checking for a hop.

In our calculations, we used a Bulirsch–Stoer (BS) integrator⁴¹ with polynomial extrapolation, as in earlier work.¹⁷ In order to make the following discussion clearer, we briefly describe this integrator. The BS integrator takes a large step of size H that is composed of many smaller modified midpoint⁴¹ steps. The BS integrator first steps through the interval H with the modified midpoint integrator using a fixed step size of $H/2$. We label the result of this calculation f_2 . The BS integrator then steps through the interval H again using a fixed step size of $H/4$; we label the result of this calculation f_4 . The quantities f_2 and f_4 are fit to a polynomial as a function of step size, and the value of the polynomial at zero step size is labeled g_1 . This is the BS integrator's first estimate of the integrated equation. To calculate the error in g_1 , the interval H is divided into six steps; the result of this calculation is labeled f_6 . The quantities f_2 , f_4 , and f_6 are again fit to a polynomial as a function of step size, and the value of this new polynomial at zero step size is labeled g_2 . If the difference between g_2 and g_1 is smaller than the tolerance parameter ϵ_{BS} , then the integrator takes g_2 as its final value and it proceeds to the next step. Otherwise, the integrator continues dividing H into smaller and smaller segments, fitting these results to polynomials and extrapolating to zero step size. Should the difference between estimates g_7 and g_8 be greater than ϵ_{BS} , the integrator decides that H is too large and it starts again with a smaller interval, $H/2$. Should a value of $H/2$ ever become smaller than an input parameter, h_{min} , then the interval is simply taken with the modified midpoint integrator in two steps. Note that the criteria for accepting a step depends upon

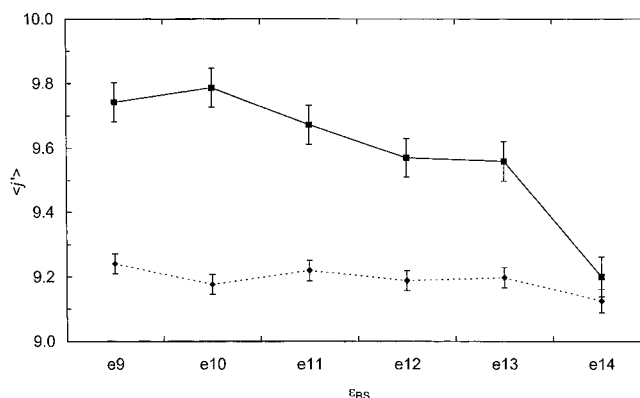


Figure 8. Final rotational moment versus the integrator tolerance ϵ_{BS} . The symbols are the same as for Figure 7.

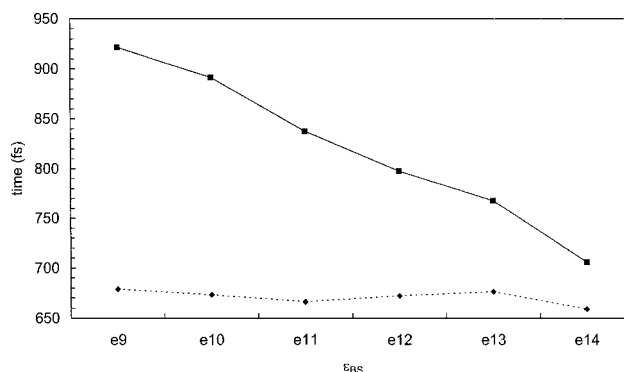


Figure 9. Time of the first surface hop versus the integrator tolerance ϵ_{BS} . The symbols are the same as for Figure 7.

the difference between subsequent values of g_i and g_j , differing by less than ϵ_{BS} for all of the equations being integrated. Thus, if a particular equation is difficult to integrate, all of the remaining equations will be integrated with smaller step sizes.

The Bulirsch–Stoer integrator proved to be very accurate. We generally obtained energy conservation to within 10^{-9} eV, and we obtained angular momentum conservation to within $10^{-9} \hbar$ at a tolerance of 5×10^{-13} . Note that ϵ_{BS} is given in the same units as the quantity being integrated, i.e., ϵ_{BS} has units of a_0 for the integration of coordinates, and it has units of \hbar/a_0 for the integration of momenta. At a larger tolerance of 10^{-9} , we obtained energy and angular momentum conservation to within 10^{-6} eV and $10^{-7} \hbar$, respectively. Despite this, we had difficulty converging the final average vibrational and rotational quantum numbers with respect to ϵ_{BS} . Figures 7 and 8 show these values for calculations at 2.030 eV using the TFS-**d** method as a function of ϵ_{BS} . Notice that the average vibrational quantum number as calculated by method I steadily increases with decreasing tolerance, while the average rotational quantum number as calculated by method I decreases with decreasing tolerance (method II is a more accurate integration method which will be discussed below). A clue to this behavior was found in a plot of the average time of the first hop, which is shown in Figure 9. Note that trajectories hop earlier as the tolerance is decreased. The energy and angular momentum are still converged to a small degree in these calculations. This suggests that the lack of stability of $\langle v \rangle$ and $\langle j \rangle$ is not an integrator error but that it is an error in the method used to calculate surface hopping probabilities.

The method we first attempted to use to calculate surface hopping probabilities is the implementation of the TFS method recommended for large time steps:⁴²

$$g_{kj} = \frac{\int_t^{t+\Delta t} dt b_{jk}(t)}{a_{kk}(t)} \quad (51)$$

where g_{kj} is the probability of a surface transition from state k to state j , Δt is an interval of time, $a_{kk}(t)$ is the probability of being in state k at time t , and

$$b_{jk}(t) = -2 \operatorname{Re}(a_{jk}^* \dot{\mathbf{R}} \cdot \mathbf{d}_{jk}) \quad (52)$$

where a_{jk} is the electronic coherence between states j and k . Note that we follow Tully's original method and never reset the electronic coherence during the calculation of a trajectory.⁵ For a two-state system,

$$b_{12}(t) = \dot{a}_{11}(t) \quad (53)$$

and

$$b_{21}(t) = \dot{a}_{22}(t) \quad (54)$$

and the hopping probabilities become

$$g_{21} = \frac{a_{22}(t) - a_{22}(t + \Delta t)}{a_{22}(t)} \quad (55)$$

and

$$g_{12} = \frac{a_{11}(t) - a_{11}(t + \Delta t)}{a_{11}(t)} \quad (56)$$

Note that only one of g_{21} or g_{12} can be positive; the negative valued hopping probability is set to zero.

The TFS method requires small steps, since it is based on the time derivative of the electronic state probabilities. The BS integrator, however, is designed to take large steps. There is thus a mismatch between these two components. Figure 10 shows a plot of the function $a_{22}(t)$ calculated in two different ways. The open circles represent steps taken during the course of integrating $b_{21}(t)$ with the BS integrator described above. This is called method I. The solid lines are drawn to connect the circles. The pluses represent the results of integrating $b_{21}(t)$ in a fashion that required it to take small steps near extrema in $a_{22}(t)$ (zeros in $b_{21}(t)$). This method will be discussed below, and it is called method II. The dashed lines are drawn to connect the pluses in Figure 10. Note that the two methods agree; the locations of the open circles always occur on the dashed lines. The difference is that method I is able to accurately take larger steps. This allows it to partially bypass the peaks and valleys in the electronic probabilities. These extrema are probably well-approximated by second-order polynomials, which the modified midpoint integrator can integrate exactly. It can thus cross the peaks without reducing the interval H . This is an efficient method of integration, but it results in an incorrect calculation of the hopping probability. Consider the interval labeled by a and b in Figure 10. According to eq 55, the probability of hopping from surface 2 to surface 1 with method I over the interval ab is $(0.99854 - 0.99848)/0.99854 = 6.0 \times 10^{-5}$. On the other hand, if we integrate the trajectory with method II, the integrator must first step to a point b' , for example. The probability of hopping is different. The probability for hopping over the interval ab' is $(0.99854 - 0.99789)/0.99854 = 6.5 \times 10^{-4}$, and the probability of hopping over the interval $b'b$ is zero. These calculations differ by an order of magnitude. Note that the hopping probability calculated by method I is smaller

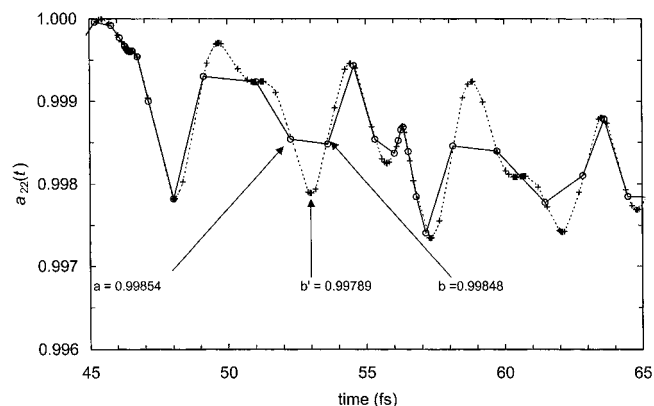


Figure 10. $a_{22}(t)$ versus time. The open circles linked by solid lines represent values obtained through integration of $b_{21}(t)$ by method I. The pluses linked by dotted lines represent values obtained through integration of $b_{21}(t)$ with method II.

than the probability calculated by method II; the effect of integrating through the peaks and the valleys with method I is to smooth the changes in the electronic probabilities, which reduces the calculated hopping probabilities. We should point out that the TFS method is formally independent of step size. In the example given above, the state populations at time b for both methods should be identical, since in method II some of the trajectories on the lower surface that hopped down in the interval ab' should hop back up in the interval $b'b$. In actuality, trajectories on the lower electronic surface need not follow the same paths that trajectories on the excited surface do, and in the present example, trajectories that reach the lower surface tend to rapidly dissociate instead of remaining in the interaction region and hopping back up.

In a typical system, this small error in the calculation of the hopping probabilities would not tend to result in a systematic error in the final trajectory attributes. However, in the current system, there are two characteristics that exacerbate this error. First, the nonadiabatic coupling vector is never large, so the electronic probabilities change by only a small amount during the trajectories lives. For example, in calculations with the TFS- \mathbf{d} method at 2.030 eV, the average probability for being on the upper surface at the end of a trajectory was 0.91. Second, the energy of the trajectory in the 000 and 010 states is insufficient to allow it to dissociate on the upper electronic surface. In order to dissociate, trajectories in these states must quench. These trajectories typically spent a long time in the exciplex before hopping. For example, using the TFS- \mathbf{d} method at 2.030 eV, the lifetime of the trajectories was 0.59 ps, while the total integration time was 0.90 ps. These long times combined with small probability changes seem to make the trajectories more sensitive to small errors in the hopping probability.

Decreasing ϵ_{BS} makes the peaks slightly less well-approximated by a second-order function, so the integrator cannot take as large a step through it. This reduces the error in the hopping probabilities, and it explains the trends of the final trajectory attributes with ϵ_{BS} as shown in Figures 7–9. Ultimately, decreasing the tolerance should result in converged final quantities. This brute force method is unattractive for several reasons. First, this is an indirect method for obtaining convergence of the hopping probabilities. The trajectories converge slowly with respect to ϵ_{BS} , as evidenced in Figures 7–9. The computational effort required to converge these quantities with respect to ϵ_{BS} is very large. We reiterate that the accuracy of the integrator is not an issue here; the error in

the hopping probability occurs between successive integration steps. Second, decreasing the tolerance means that the integrator must integrate all of the remaining equations more accurately. This could force the integrator to use small step sizes even in regions where $b_{21}(t)$ is not changing rapidly. Finally, it should be mentioned that the error in the calculation of the hopping probability is not limited to the BS integrator but that this error will occur in any high-order adaptive step size integrator. Since these integrators in general will have different criteria for adjusting their step sizes, it is important to find a general method that is widely applicable.

A subtle alternative is to prohibit the integrator from stepping over peaks and valleys in the electronic probabilities. We accomplished this by dividing the quantity $b_{jk}(t)$ in eq 51 into positive and negative components and then integrating them separately:

$$b_{jk}^+(t) = \max[b_{jk}(t), 0] \quad (57)$$

$$b_{jk}^-(t) = \min[b_{jk}(t), 0] \quad (58)$$

$$g_{kj} = \frac{\int_t^{t+\Delta} dt b_{jk}^+(t) + \int_t^{t+\Delta} dt b_{jk}^-(t)}{a_{kk}(t)} \quad (59)$$

This is called method II. The integral over $b_{jk}^+(t)$ in eq 59 is a function that either increases with time or remains constant with time, but it never decreases with time. Similarly, the integral over $b_{jk}^-(t)$ in eq 59 is a function that never increases with time. Thus, neither peaks nor valleys appear in either of the integrals in eq 59. The functions $b_{jk}^+(t)$ and $b_{jk}^-(t)$ are continuous everywhere, but all of their derivatives are discontinuous when $b_{jk}(t)$ equals zero. The BS integrator has difficulty in its extrapolation step when it crosses this point. Consequently, it reduces the step size in this region, as is evidenced by the clustering of points near the extrema in Figure 10. The improved convergence obtained with this method is illustrated in Figures 7–9 by dotted lines. We note that any other high-order adaptive step size integrator will also have difficulties stepping through points where $b_{jk}(t)$ is zero, and therefore, eqs 57–59 are generally applicable.

We should point out that although it may be more straightforward to converge fixed-step integrators with respect to step size than to converge variable step size integrators, we have found that the current system requires very small fixed step sizes and that the BS integrator with the adaptive step size control is more efficient. For systems with larger changes in $b_{jk}(t)$, the adaptive step size modification is unnecessary, and it is clear that in this case variable step size integrators will be even more efficient. Apart from efficiency issues, an important aspect of the adaptive step size control described above is that it frees the TFS method from integrator dependence, even for systems with small hopping probabilities.

For our final calculations, we used values of ϵ_{BS} equal to 5×10^{-13} and h_{min} equal to $10^{-4} a_0$. Twenty-eight percent of all the trajectories at all energies took steps smaller than h_{min} with the TFS-d method. These trajectories took an average of 1.6 modified midpoint steps.

In addition to converging the final trajectory attributes with respect to the numerical parameters ϵ_{BS} and h_{min} , we converged them with respect to the number of trajectories we calculated. We calculated the statistical error by performing 10 000 trajectory calculations at each energy and with each of the 4 trajectory methods. We then randomly divided each group of

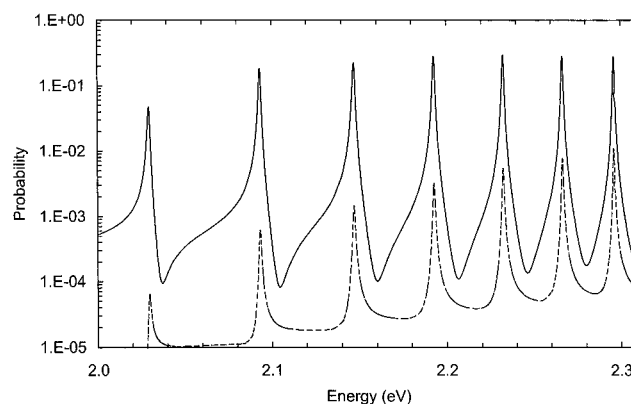


Figure 11. Quantum mechanical probability of a transition from the $\text{Na}(3s) + \text{H}_2(0,j)$ state to any $\text{Na}(3s) + \text{H}_2(2,j')$ states. The solid line indicates $j = 10$, and the dotted line indicates $j = 2$.

TABLE 5: Average Statistical Uncertainty in the Calculated Values

	TFS-d	rotated TFS-d	TFS-g	rotated TFS-g
$\langle \nu \rangle$	0.013	0.016	0.014	0.011
$\langle j \rangle$	0.052	0.064	0.066	0.048
τ , ps	0.006	0.019	0.007	0.015

10 000 trajectories into 4 sets of 5000 trajectories (by considering the first 5000, the second 5000, the odd 5000, and the even 5000), and we calculated the standard deviation from the mean for the average final vibrational and rotational quantum numbers and for the lifetimes for each of the 4 groups. Table 5 presents the standard deviation averaged over all seven energies for each method. This table implies that 10 000 trajectories is sufficient for meaningful results.

We also checked the convergence of $\langle \nu' \rangle$, $\langle j' \rangle$, and τ with respect to the final separation between Na and H_2 when we stopped integrating the trajectory. Na and H_2 must have a separation large enough that there are no interactions between them in order for the final state analysis to be correct. To test that this criterion was being satisfied, we performed a set of 10 000 trajectories with the TFS-d method at 2.03 eV, and we ended the integration at separations of 10, 15, and 20 Å. Neither $\langle \nu' \rangle$, $\langle j' \rangle$, nor τ showed dependence on this parameter. For our final calculations, we ended the integration when the final separation was larger than 15 Å.

All of our TSH calculations were carried out in the adiabatic representation, as recommended by Tully.^{15,16}

5. Results

We calculated the accurate quantum mechanical probabilities for an H_2 molecule in the $\nu = 0$, $j = 10$ state and in the $\nu = 0$, $j = 2$ state to collide with $\text{Na}(3s)$ and experience a transition to any $\nu' = 2$ state as a function of energy. This is shown in Figure 11. Note the appearance of resonances corresponding to the formation of NaH_2 exciplexes.

For the TFS methods, the histogram method,^{10,43} linear smooth sampling (LSS) method,^{10,43–46} and quadratic smooth sampling (QSS)^{10,47} method were used to assign final vibrational and rotational states. We found that the differences between these three methods were negligible, and therefore, we present only the histogram results.

In all of the semiclassical calculations, we only included trajectories that finished on the lower surface. All seven of the energies we studied are lower than the zero-point energy of $\text{Na}(3p) + \text{H}_2(0,0)$. However, since we do not enforce the zero-point energy, five of the trajectory calculations (those beginning

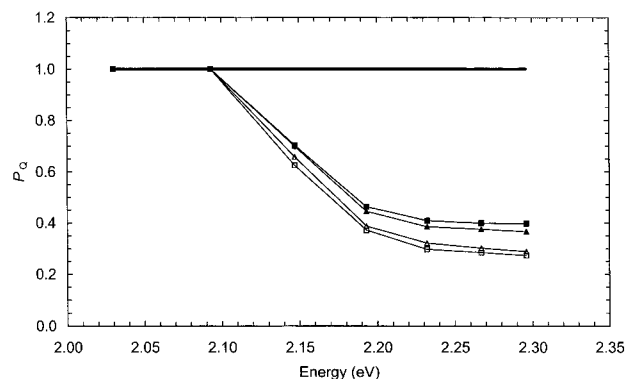


Figure 12. Quenching probability versus energy. The thick black line represents the quantum results. Squares represent **d** methods; triangles represent **g** methods. Solid symbols represent nonrotated methods, and open symbols represent rotated vector methods.

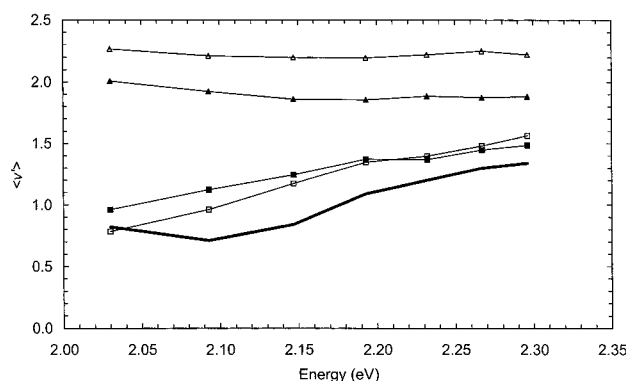


Figure 13. Final average vibrational quantum number versus the total energy. Symbols are the same as in Figure 12.

in the 020–060 states) produce products on the excited potential energy surface. We neglect trajectories that do not quench, since we are interested in comparing our results to quantum mechanical calculations, which of course cannot dissociate on the upper surface. Figure 12 illustrates the quenching probability as a function of energy.

After assigning probabilities for final states with integral quantum numbers to all trajectories, we used these probabilities to calculate the final average vibrational and rotational quantum numbers for the product $\text{H}_2(\nu', j')$ for each batch of trajectories. These averages are defined in eqs 20 and 21. Figures 13 and 14 show plots of $\langle \nu' \rangle$ and $\langle j' \rangle$, respectively, for all four semiclassical methods and compares them to the accurate quantum mechanical calculations. We also calculated the average final relative energy of the products for each batch of trajectories. Figure 15 shows the average final relative energy of the products for each of the semiclassical calculations.

We obtained the lifetimes of the resonances from our quantum mechanical calculations according to eq 22. In order to obtain the corresponding quantities from our TSH calculations, we first calculated the delay time⁴⁸ for each trajectory, which is a measure of the amount of time two particles interact with other. Let $T(\rho', E)$ be the amount of time it takes for an exciplex with energy E to decay into products $\text{Na}(3s) + \text{H}_2(\nu', j')$ moving at a final relative velocity of ν'_{rel} to reach a separation ρ' . The quantity ρ'/ν'_{rel} is approximately the time it would have taken two noninteracting particles to travel the same distance. The difference of these two times, in the limit of infinite separation, is the delay time:

$$t_d(\rho', E) = \lim_{\rho' \rightarrow \infty} [T(\rho', E) - \rho'/\nu'_{\text{rel}}] \quad (60)$$

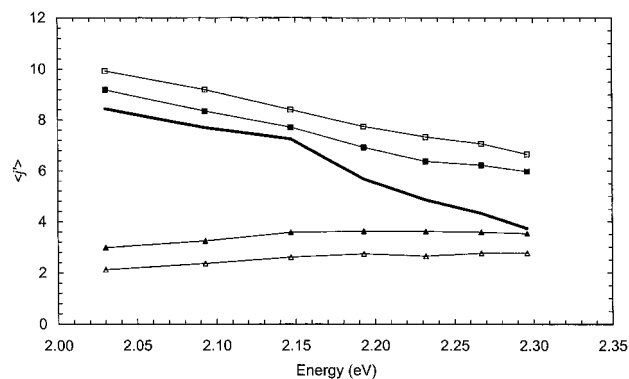


Figure 14. Final average rotational quantum number versus the total energy. Symbols are the same as in Figure 12.

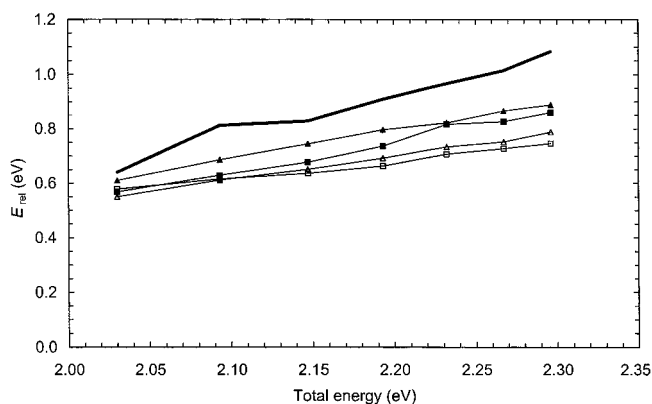


Figure 15. Average final relative energy versus the total energy. Symbols are the same as in Figure 12.

This definition is different than in earlier work^{9,17,49} in that the initial velocity and distance is not present in the limit in eq 59. This is because we are performing calculations for a unimolecular decay reaction rather than for a bimolecular collision.

In order to determine the lifetimes of the semiclassical unimolecular decay states, we plotted the number of undecayed exciplexes versus the delay time on a semi-log plot. This plot shows noise for large delay times because there are only a few undecayed exciplexes remaining. For small delay times, the decay is not expected to be statistical. Therefore, we fit the center third of the distribution to a straight line as a function of the delay time. The negative inverse of the slope of this line gives τ , the lifetime of the exciplex. We note that this definition of the lifetime is the appropriate one for comparison to the lifetime given by eq 22; it can be shown that τ is the mean lifetime for exponential decay.³⁴ Figure 16 shows the semiclassical mean lifetimes and compares them to the calculated quantum mechanical lifetimes.

Table 6 presents the overall root-mean-square (RMS) errors for the four semiclassical methods for each of the four quantities we calculated: the average final vibrational and rotational quantum numbers, the mean lifetimes, and the final average relative energies. The absolute RMS error is defined as

$$\text{Err}_{\text{abs}} = \sqrt{\langle (\text{error})^2 \rangle} \quad (61)$$

and the relative RMS error is defined as

$$\text{Err}_{\text{rel}} = \sqrt{\left\langle \frac{(\text{error})^2}{(\text{accurate quantum mechanical value})^2} \right\rangle} \quad (62)$$

where the average in both cases is over the seven resonance energies.

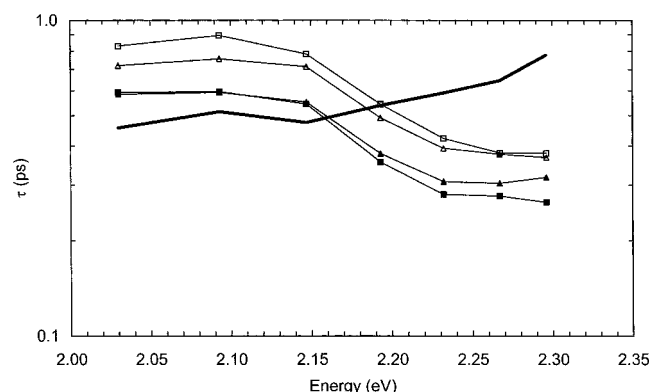


Figure 16. Mean lifetime versus the total energy. Symbols are the same as in Figure 12.

TABLE 6: Semiclassical RMS Errors in the Mean Lifetime, in the Final Vibrational Moment, in the Final Rotational Moment, and in the Average Final Relative Energy for Potential Matrix 6^a

	TFS-d	rotated TFS-d	TFS-g	rotated TFS-g
absolute RMS Errors				
τ , ps	0.28	0.30	0.26	0.26
$\langle v' \rangle$	0.27*	0.23*	0.89	1.20
$\langle j' \rangle$	1.40*	2.15*	3.15	3.90
$\langle E_{\text{rel}} \rangle$, eV	0.17*	0.24*	0.13*	0.22*
relative RMS Errors				
τ , ps	43	55	39	44
$\langle v' \rangle$	32*	24*	105	36
$\langle j' \rangle$	32*	46*	42	55
$\langle E_{\text{rel}} \rangle$, eV	18*	25*	14*	23*

^a Bold numbers indicate the lowest error for each of the four quantities. Asterisks indicate calculations in which the quantum mechanical trend of the quantity with energy is reproduced by the semiclassical method.

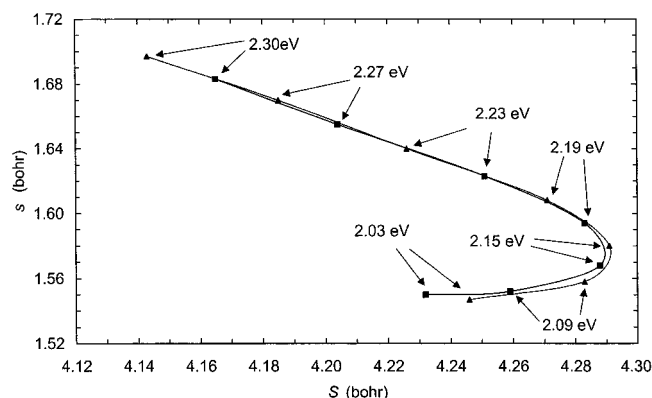


Figure 17. Average hopping location as a function of S and s . In this plot, χ is equal to 90° , which is the angle of the average hop. Solid squares represent TFS-d calculations, and solid triangles represent TFS-g calculations.

We examined the hopping events of the semiclassical methods in more detail in order to describe trends that appear in the final product distributions as the energy is increased. Figure 17 illustrates the average locations of hops for the TFS-d method and for the TFS-g method. Figure 18 illustrates the distribution of energy changes in the three vibrational modes at the time of hopping for the TFS-d and TFS-g methods at 2.030 eV. Figure 19 illustrates the \hat{w} and \hat{y} components of \mathbf{d} and \mathbf{g} (defined in Appendix B) versus energy. At each energy, these components were calculated at S and s values corresponding to the average hopping location. For this plot, χ was chosen to be equal to 80° , since the vector \mathbf{d} is undefined when χ equals 90° . Figure

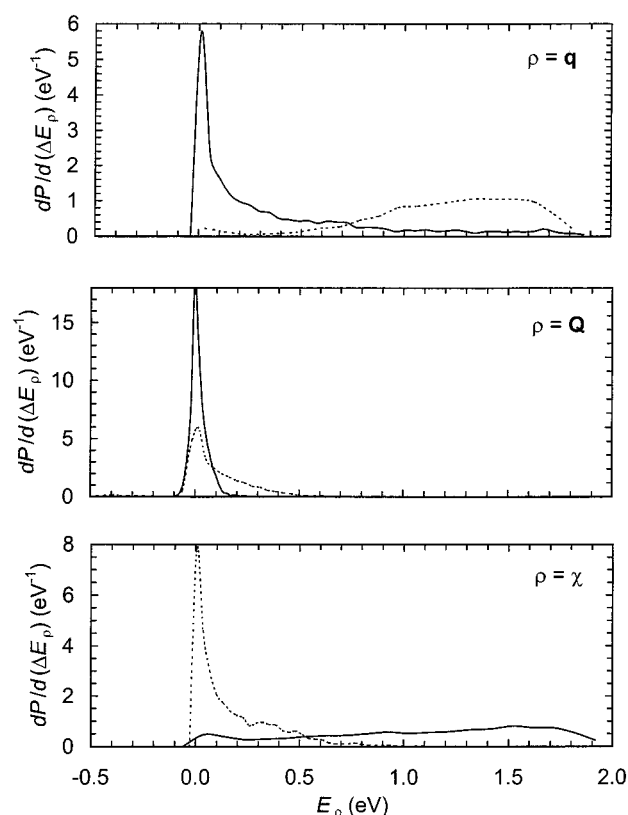


Figure 18. Distributions of the change in energy along each mode during hops for the TFS-d and TFS-g methods. Solid lines represent the TFS-d method, and dotted lines represent the TFS-g method.

20 shows a plot of the average energy gap during a hop; Figure 21 shows a plot of the average kinetic energy at the time of a hop.

We also examined the rotated method in detail. In particular, we are interested in how the rotated vector methods differ from their nonrotated counterparts. Figure 22 shows the percentage of trajectories that experienced one or more rotations of the hopping vector. Figure 23 shows the average angle the hopping vector needed to be rotated in order to allow a hop.

6. Discussion

The semiclassical methods will be unable to predict the characteristic resonance behavior illustrated, for example, in Figure 11. Presumably, semiclassical predictions of these collisional transition probabilities would be a smoothly changing function of energy that would be an average of the resonant behavior shown in Figure 11. However, Figure 11 illustrates that at certain energies $\text{Na}(3s)$ and $\text{H}_2(v,j)$ may form quasi-bound exciplexes that serve to redistribute energy between vibration and rotation. With this interpretation of the resonance behavior, we model the decay of the exciplexes directly by beginning the semiclassical calculations in the intermediate quasi-bound states. In a sense, we bypass the purely quantum aspect of these resonances, which is that these exciplex states are quantized and are only formed at particular energies. We ask three questions of these trajectory calculations. First, which method does the best at describing the quantum mechanics calculations? Second, when the TFS-d and TFS-g methods differ substantially, why do they differ? Third, what effect does the rotation of the hopping vector have on final trajectory quantities?

Examination of Figures 13 and 14 shows that the TFS-d and rotated TFS-d methods do better than the TFS-g and rotated TFS-g methods do at describing the trend of $\langle v' \rangle$ and $\langle j' \rangle$ with

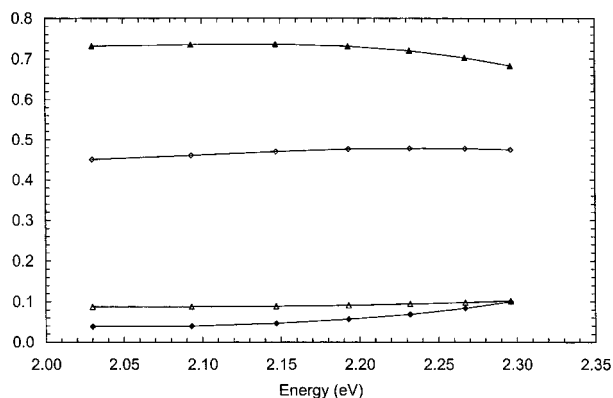


Figure 19. \hat{y} and \hat{w} components of \hat{d} and \hat{g} versus energy. Solid symbols represent the \hat{d} vector, and open symbols represent the \hat{g} vector. Diamonds represent the \hat{y} component, and triangles represent the \hat{w} component. At each energy, \hat{d} and \hat{g} were calculated at a geometry near the average hopping location. In this plot, S and s are equal to the average values of S and s during hopping events. The angle χ , however, is not set equal to 90° , which is the average hopping value of χ , but is instead set equal to 80° .

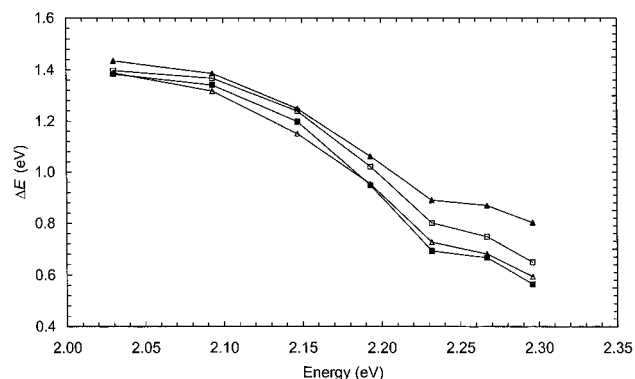


Figure 20. Average energy gap between the two adiabatic surfaces at hopping events. Symbols are the same as in Figure 12.

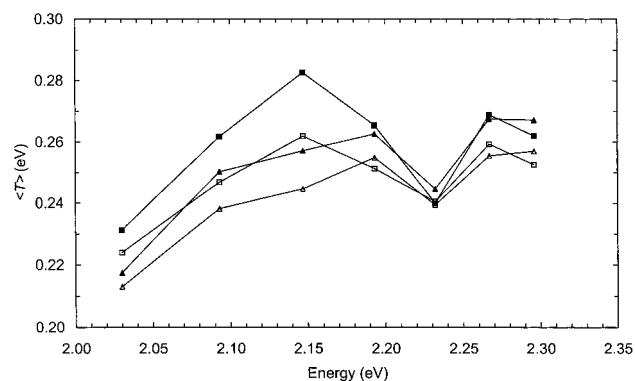


Figure 21. Average kinetic energy at hopping events. Symbols are the same as in Figure 12.

the total energy. The TFS-g and rotated TFS-g methods give final average quantum numbers that are nearly independent of energy.

All of the semiclassical methods correctly describe the trend of the quantum mechanical relative energies to increase with increasing total energy (Figure 15). The TFS-g method has the smallest error, and the TFS-d method is slightly higher than this. The rotated methods both show a decreased amount of average final relative energy than their nonrotated counterparts.

None of the TFS methods show the same trend of the lifetime to increase as a function of energy as the quantum methods. This is probably related to the zero-point energy of the Na(3p)

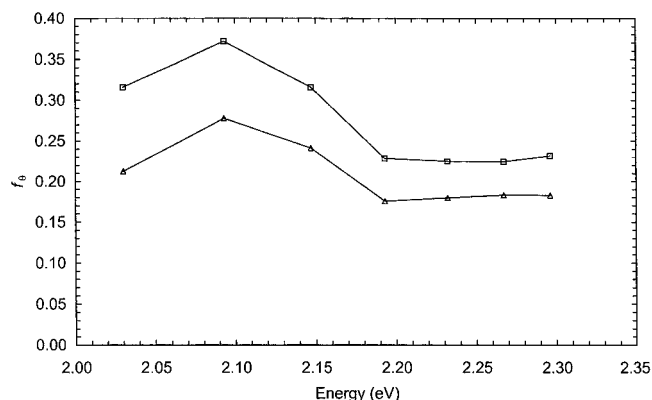


Figure 22. Fraction of trajectories that experienced one or more hopping vector rotation. Open squares represent the rotated TFS-d method; open triangles represent the rotated TFS-g method.

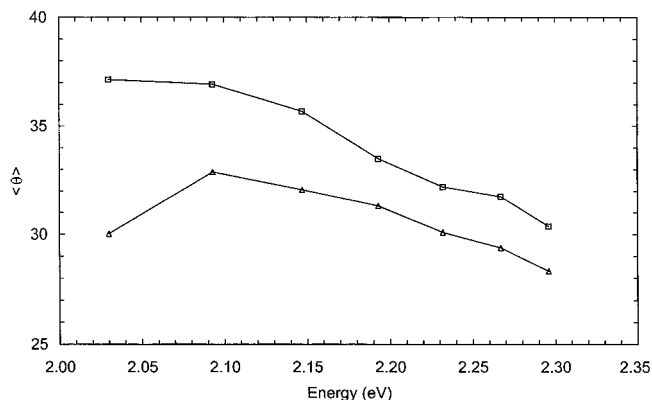


Figure 23. Average value of the angle of vector rotation for those trajectories that experienced at least one rotation. The symbols are the same as for Figure 21.

+ H₂(0,0) channel, which opens at 2.373 eV. The classical methods do not enforce zero-point energy, so above 2.104 eV, where the classical Na(3p) + H₂ asymptote becomes energetically accessible, some trajectories dissociate on the upper surface rather than hop. The incorrect trend of τ with energy is also related to the hopping probabilities, which tend to be very small. Trajectories are more likely to dissociate on the upper surface long before a hop occurs, if energy permits. It can be seen in Figure 12 that only a small fraction of the trajectories quench at high energies. If zero-point energies were enforced, however, higher energy trajectories would be prevented from dissociating, and they would hop down after oscillating on the upper surface for some time. These trajectories would then add their longer decay times to the population, and the calculated mean lifetimes should increase. We have not tested this prediction.

For the 000 and 010 states, however, zero-point-energy conservation does not have such a pronounced effect. If we consider only these two states, it is clear that the rotated methods predict a lifetime that is too high.

Table 6 summarizes the absolute errors of the semiclassical methods and their ability to reproduce the trends that the quantum mechanical calculations show. All of the methods reproduce the trend of the average final relative energy to increase with increasing total energy. The TFS-g method has the lowest error in the calculation of the average final relative energy, but the error of the TFS-d method is only slightly larger. The TFS-d and rotated TFS-d methods are the only methods that correctly describe the trends of the average vibrational and rotational quantum numbers with energy. The absolute errors of these two methods for the final vibrational quantum numbers

are comparable, but the TFS-**d** method has a much smaller error in the average final rotational quantum number. None of the methods reproduces the trend of the final lifetime, and all of the errors are roughly comparable. For these reasons, we believe that the nonrotated TFS-**d** method is the best method for this system.

An examination of the hopping events may indicate how the differences in the final products result. In Figure 17, we can see that as energy is increased, both the TFS-**g** and TFS-**d** methods show similar changes in the average hopping location. This similarity indicates that the hopping location alone is not sufficient to account for the different dynamics observed with each method.

The difference in the final product distribution can be understood by examining the changes in momentum during the hopping event. In Figure 15, we see that the **d** vector tends to have the largest component along $\hat{\mathbf{w}}$, while the **g** vector has the largest component along $\hat{\mathbf{y}}$. This explains why the TFS-**g** method and the rotated TFS-**g** method show a much higher $\langle \nu' \rangle$ and a much lower $\langle j' \rangle$ than the TFS-**d** method and the rotated TFS-**d** method do. Neither the TFS-**d** method nor the TFS-**g** method shows much change in energy along $\hat{\mathbf{Y}}$.

The trends of $\langle \nu' \rangle$ and $\langle j' \rangle$ with energy shown in Figures 13 and 14 are likely caused by a change in the orientation of the **d** and **g** vectors with geometry. This is illustrated in Figure 19. Note that the largest component of the **d** vector lies along $\hat{\mathbf{w}}$ and that this component becomes smaller as the energy increases. This correctly describes the trend illustrated by the TFS-**d** calculations in Figure 14, which shows that the average rotational quantum number decreases as the energy increases. The component of the **d** vector along $\hat{\mathbf{y}}$, on the other hand, increases. This agrees with the trend of the TFS-**d** method shown in Figure 12, which shows that the average vibrational quantum number increases as the energy decreases. The components of the **g** vector remain relatively independent of energy, which agrees with the trends of the TFS-**g** method illustrated in Figures 13 and 14. It thus appears that in this system, the final energy distributions are determined by the orientation of the hopping vectors at the moment of hopping.

This suggests that the redistribution of internal energy by the exciplex is negligible by comparison. One might wonder, for example, whether trajectories that spent a longer amount of time in the exciplex prior to hopping systematically accumulated energy in any particular vibrational mode. We investigated this possibility by dividing our batches of 10 000 trajectories into 3 groups according to the time of their first surface hop. We calculated $\langle \nu' \rangle$ and $\langle j' \rangle$ for each group, and we discovered that there was no correlation between how long trajectories spent in the exciplex prior to the first hop and the final energy distribution. The large average energy gap at the moment of hopping is probably the reason for this. As seen in Figures 20 and 21, the average energy gap is about 1.0 eV, while the amount of kinetic energy prior to a hop is only about 0.25 eV. Tully has suggested that the ratio of these two energies is an indication of how accurate TSH methods might be.⁵⁰ In this situation, it seems to indicate how sensitive the final products will be to the method used to adjust the momentum during the hopping event. Other systems with smaller average energy gaps may show less dependence on the choice of vector used to adjust the momentum at the moment of hopping. Thus, in earlier studies,^{9,10} it is possible that the **d** vector and the **g** vector pointed in different directions but that the small energy gap at hopping events made this difference negligible.

The rotated vector methods show many systematic differences from the nonrotated methods. For example, the rotated TFS-**d** method predicts a systemic increase in $\langle j' \rangle$ from the nonrotated TFS-**d** prediction, while the rotated TFS-**g** method predicts a systematic decrease in $\langle j' \rangle$ and an increase in $\langle \nu' \rangle$ from the nonrotated TFS-**g** prediction. The rotated methods also seem to shift the final average relative energy to lower values. We can understand these trends in terms of Figure 18. For example, if a rotated TFS-**d** trajectory hops to a lower energy surface, roughly 1.0 eV of the potential energy is converted into kinetic energy in the rotational coordinate, according to Figure 18. If, at a later time, this trajectory attempts a hop with insufficient momentum along **d**, this probably indicates that the energy which had recently been deposited in the rotational mode has become partitioned into mostly potential energy. By rotating the **d** vector, we allow the kinetic energy in other modes to be used to hop up. At a later time, the trajectory will again hop down and more kinetic energy will be added into the rotational mode. Thus, rotating the hopping vector has the effect of taking energy out of modes that are not associated with the nonrotated hopping vector and adding that energy into modes that are associated with the nonrotated hopping vector. In Figures 13 and 14, we see that the rotated TFS-**g** method has added energy into the vibrational mode and removed it from the rotational mode. The rotated TFS-**d** method, on the other hand, has added energy to the rotational mode and removed it from the translational coordinate, as can be seen in Figures 13 and 15. We can see in Figures 22 and 23 that a larger number of trajectories experience momentum prohibited hops in this system and also that the **d** or **g** vector is rotated by a fairly large angle when these hops occur. The strong effect that rotation has in this system is probably related to the large energy gap during hopping events.

The rotated vector methods also show systematic trends that seem less dependent on the choice of hopping vector. The increase in the mean lifetime and the decrease in quenching probability over the nonrotated methods are two examples. In both cases, the effects stem from the small hopping probabilities in the current system. The lifetime is increased because trajectories that hop back to the excited surface will spend a long time trapped in the exciplex before hopping again. At higher energies, trajectories that hop back up are more likely to dissociate on the excited surface rather than hop back down, and as a result, the quenching probabilities decrease.

These effects are likely to worsen if energetically forbidden surface hops are allowed to occur. In the TFS-**d** calculations at 2.032 eV, for example, 85% of the trajectories experienced at least one energy-prohibited hop, and the average number of energy-prohibited hops was 3.8. On the other hand, only 32% of the trajectories experienced at least one momentum-prohibited hop, and the average number of momentum prohibited hops was 1.3. Correcting the energy problem might drastically increase the lifetime at low energies and decrease the quenching probability at higher energies. In these cases, it is possible that hops should not have occurred in the first place. It could be a shortcoming in the quantum path equations that the electronic probabilities change in regions where hops cannot occur. This may suggest a strategy of building the energy criteria and the momentum criteria into the quantum path equations themselves, instead of devising methods to correct hopping failures.

As a final note, we reiterate the features in this system that make accurate semiclassical calculations difficult. The electronic probabilities change by a very small amount over the life of the trajectories. Thus, the hopping probability at each integration

step is very small and is more sensitive to errors. Second, the low-energy trajectories spend a long time in the exciplex before dissociating, causing these errors in the hopping probability to accumulate. Third, zero-point energy is not conserved, and higher energy trajectories can dissociate without quenching on the upper surface. Finally, the final products seem to be very sensitive to the direction that the hopping vector points, due to the large energy gap in this system. Despite these difficulties, the semiclassical calculations show qualitative agreement with quantum mechanical calculations.

7. Concluding Remarks

We have presented quantum mechanical scattering calculations at energies associated with NaH₂ exciplex resonance states. These calculations provide the total and partial widths of the resonances, and they allow the determination of their lifetimes and of the final average rotational and vibrational numbers of the products of decay. We have used trends in the energy spacings, lifetimes, and product-state distributions to assign the resonances. We compared these results with trajectory surface hopping calculations employing Tully's fewest switches algorithm with four different directions for adjusting the momentum at the time of a hop (this direction is called the hopping vector). The TFS-**d** method (which uses the prescription originally suggested by Preston and Tully) and the TFS-**g** method (which uses the prescription originally suggested by Blais and Truhlar) give very different results. The two other methods, TFS rotated-**d** and TFS rotated-**g**, are new in this paper. It is shown that the TFS-**d** and the rotated TFS-**d** methods describe the trends in $\langle \nu' \rangle$ and $\langle j' \rangle$ with energy much better than the TFS-**g** or rotated TFS-**g** methods do. None of the four methods correctly describes the trend of the lifetimes with energy. The rotated-vector methods show several systematic changes in the computed final quantities from their nonrotated counterparts, and rotation of the hopping vector has a strong effect on the energy distributions. Nevertheless, although rotation provides a solution to the coupled nuclear-electronic dynamics that preserves the self-consistency of the ensemble averages better than not rotating, it does not *systematically* improve the calculated values of physical observables. In fact, the strong systematic changes caused by rotation tend to increase the average errors, and therefore we believe the nonrotated TFS-**d** method is the best method for the present system. This is the first time we have found a system where the results of choosing the **d** and **g** directions of the hopping vector are different. Hence, this provides the first numerical evidence that either method is superior to the other.

We have also presented an adaptive integration scheme for the TFS method that allows hopping probabilities to be calculated more accurately. This adaptive integrator is essential for systems like the present one, which has very small changes in the electronic probabilities.

Acknowledgment. This work was supported in part by the National Science Foundation under Grant No. CHE97-25965.

Appendix A

This appendix summarizes the numerical methods used to calculate $\mathbf{d}_{12}(\mathbf{R})$ and $\mathbf{g}_{12}(\mathbf{R})$. In the calculation of both of these vectors, only the diabatic potential matrix elements $U_{11}(\mathbf{R})$, $U_{12}(\mathbf{R})$, and $U_{22}(\mathbf{R})$ and their gradients are required.

We calculate the nonadiabatic coupling vector between two adiabatic states $\phi_1^a(\mathbf{x};\mathbf{R})$ and $\phi_2^a(\mathbf{x};\mathbf{R})$ with the Hellmann–Feynman expression

$$\nabla_{\mathbf{R}} \langle \phi_i^a(\mathbf{x};\mathbf{R}) | H^{\text{el}}(\mathbf{x};\mathbf{R}) | \phi_j^a(\mathbf{x};\mathbf{R}) \rangle = \langle \phi_i^a(\mathbf{x};\mathbf{R}) | \nabla_{\mathbf{R}} H^{\text{el}}(\mathbf{x};\mathbf{R}) | \phi_j^a(\mathbf{x};\mathbf{R}) \rangle - [E_j(\mathbf{R}) - E_i(\mathbf{R})] \langle \phi_i^a(\mathbf{x};\mathbf{R}) | \nabla_{\mathbf{R}} \phi_j^a(\mathbf{x};\mathbf{R}) \rangle = 0 \quad (\text{A1})$$

which gives

$$\mathbf{d}_{12}(\mathbf{R}) = \frac{\langle \phi_1^a(\mathbf{x};\mathbf{R}) | \nabla_{\mathbf{R}} H^{\text{el}}(\mathbf{x};\mathbf{R}) | \phi_2^a(\mathbf{x};\mathbf{R}) \rangle}{E_2(\mathbf{R}) - E_1(\mathbf{R})} \quad (\text{A2})$$

where $H^{\text{el}}(\mathbf{x};\mathbf{R})$ is the electronic Hamiltonian and the adiabatic energies $E_1(\mathbf{R})$ and $E_2(\mathbf{R})$ are given by

$$E_1(\mathbf{R}) = \bar{U}(\mathbf{R}) - \sqrt{\Delta U(\mathbf{R})^2 + U_{12}^2(\mathbf{R})} \quad (\text{A3})$$

$$E_2(\mathbf{R}) = \bar{U}(\mathbf{R}) + \sqrt{\Delta U(\mathbf{R})^2 + U_{12}^2(\mathbf{R})} \quad (\text{A4})$$

where

$$\bar{U}(\mathbf{R}) = \frac{1}{2} (U_{22}(\mathbf{R}) + U_{11}(\mathbf{R})) \quad (\text{A5})$$

$$\Delta U(\mathbf{R}) = \frac{1}{2} (U_{22}(\mathbf{R}) - U_{11}(\mathbf{R})) \quad (\text{A6})$$

We expand the adiabatic wave functions in a diabatic basis

$$\phi_1^a(\mathbf{x};\mathbf{R}) = c_{11}(\mathbf{R})\phi_1^d(\mathbf{x}) + c_{12}(\mathbf{R})\phi_2^d(\mathbf{x}) \quad (\text{A7})$$

$$\phi_2^a(\mathbf{x};\mathbf{R}) = c_{21}(\mathbf{R})\phi_1^d(\mathbf{x}) + c_{22}(\mathbf{R})\phi_2^d(\mathbf{x}) \quad (\text{A8})$$

Substituting eqs A3 and A4 into eq A2 and recognizing that the gradient of the diabatic wave functions is zero (by assumption^{1,51,52}) gives

$$\mathbf{d}_{12}(\mathbf{R}) = \frac{1}{E_2(\mathbf{R}) - E_1(\mathbf{R})} \{ c_{11}(\mathbf{R})c_{21}(\mathbf{R})\nabla_{\mathbf{R}}U_{11}(\mathbf{R}) + c_{12}(\mathbf{R})c_{22}(\mathbf{R})\nabla_{\mathbf{R}}U_{22}(\mathbf{R}) + [c_{11}(\mathbf{R})c_{22}(\mathbf{R}) + c_{12}(\mathbf{R})c_{21}(\mathbf{R})]\nabla_{\mathbf{R}}U_{12}(\mathbf{R}) \} \quad (\text{A9})$$

Here, $U_{11}(\mathbf{R})$ and $U_{22}(\mathbf{R})$ are the diagonal diabatic potential matrix elements and $U_{12}(\mathbf{R})$ is the off-diagonal diabatic coupling element. The diabatic wave-function coefficients and the adiabatic energies are determined by diagonalizing the diabatic potential energy matrix. The gradients of our analytical diabatic potential matrix elements were derived with the Adifor algorithm.

The gradient of the differences in adiabatic potential energies is defined by

$$\mathbf{g}_{12}(\mathbf{R}) = \nabla_{\mathbf{R}}(E_1(\mathbf{R}) - E_2(\mathbf{R})) \quad (\text{A10})$$

Substituting eqs A3–A6 into eq A10 gives a result that can be simplified to

$$\mathbf{g}_{12}(\mathbf{R}) = \frac{2\Delta U(\mathbf{R})}{\sqrt{\Delta U(\mathbf{R})^2 + U_{12}^2(\mathbf{R})}} \nabla_{\mathbf{R}}[U_{11}(\mathbf{R}) - U_{22}(\mathbf{R})] \quad (\text{A11})$$

Appendix B

In order to decompose $\mathbf{p}_{\mathbf{R}}$ into \mathbf{p}_{vib} and \mathbf{p}_{rot} , we define five new unit vectors as follows:

$$\hat{\mathbf{z}} = \frac{\mathbf{q} \times \mathbf{Q}}{|\mathbf{q} \times \mathbf{Q}|} \quad (\text{B1})$$

$$\hat{\mathbf{y}} = \frac{\mathbf{q}}{q} \quad (\text{B2})$$

$$\hat{\mathbf{Y}} = \frac{\mathbf{Q}}{Q} \quad (\text{B3})$$

$$\hat{\mathbf{x}} = \hat{\mathbf{z}} \times \hat{\mathbf{y}} \quad (\text{B4})$$

$$\hat{\mathbf{X}} = \hat{\mathbf{z}} \times \hat{\mathbf{Y}} \quad (\text{B5})$$

Then \mathbf{p}_q and \mathbf{p}_Q can be expressed in terms of these five unit vectors as

$$\mathbf{p}_q = p_{q,x}\hat{\mathbf{x}} + p_{q,y}\hat{\mathbf{y}} + p_{q,z}\hat{\mathbf{z}} \quad (\text{B6})$$

$$\mathbf{p}_Q = p_{Q,x}\hat{\mathbf{X}} + p_{Q,y}\hat{\mathbf{Y}} + p_{Q,z}\hat{\mathbf{Z}} \quad (\text{B7})$$

where

$$p_{q,x} = \mathbf{p}_q \cdot \hat{\mathbf{x}} \quad (\text{B8})$$

$$p_{q,y} = \mathbf{p}_q \cdot \hat{\mathbf{y}} \quad (\text{B9})$$

$$p_{q,z} = \mathbf{p}_q \cdot \hat{\mathbf{z}} \quad (\text{B10})$$

$$p_{Q,x} = \mathbf{p}_Q \cdot \hat{\mathbf{X}} \quad (\text{B11})$$

$$p_{Q,y} = \mathbf{p}_Q \cdot \hat{\mathbf{Y}} \quad (\text{B12})$$

$$p_{Q,z} = \mathbf{p}_Q \cdot \hat{\mathbf{Z}} \quad (\text{B13})$$

We note that $\hat{\mathbf{x}}, \hat{\mathbf{y}}, \hat{\mathbf{z}}, \hat{\mathbf{X}}, \hat{\mathbf{Y}}, \mathbf{p}_q$, and \mathbf{p}_Q are all three-vectors. For a triatomic system in a center-of-mass coordinate system, there are 6 degrees of freedom. For noncollinear geometries, there are three vibrational modes, and these modes all lie within the triatomic plane. These modes constitute \mathbf{p}_{vib} , described above, and they do not contribute to the total angular momentum of the system. The remaining three degrees of freedom describe the rotation of the ABC molecule along three different axis, and they constitute \mathbf{p}_{rot} . These three modes determine the angular momentum of the system, and they do not change the internal coordinates of the system.

The momentum component defined by eq B9 describes the vibration of the BC bond, and thus, it is one of the components of \mathbf{p}_{vib} . The momentum component defined by eq B12 describes the vibration of the A–BC bond, and therefore, it too is a component of \mathbf{p}_{vib} . The momentum components defined by eqs B10 and B13 describe the motion of the \mathbf{q} and \mathbf{Q} vectors in a direction normal to the ABC molecular plane, and they are therefore components of \mathbf{p}_{rot} . Thus, two of the three vibrational modes and two of the three rotational axes have been specified by the coordinate system defined by eqs B1–B5 and B8–B13. There remains one vibrational mode and one rotational axis to complete the specification of \mathbf{p}_{rot} and \mathbf{p}_{vib} .

Equations B8 and B11 each describe motion that both contributes to the total angular momentum and changes the Jacobi angle χ (which is the angle between \mathbf{S} and \mathbf{s}). We take linear combinations of $p_{q,x}\hat{\mathbf{x}}$ and $p_{Q,x}\hat{\mathbf{X}}$ to form two new momenta such that one of them changes the angle χ but does not contribute to the total angular momentum and the other preserves the angle χ and does contribute to the total angular momentum. These linear combinations are given by

$$p_w \hat{\mathbf{w}} = \frac{Qp_{q,x} - qp_{Q,x}}{Q^2 + q^2} \begin{pmatrix} Q\hat{\mathbf{x}} \\ -q\hat{\mathbf{X}} \end{pmatrix} \quad (\text{B14})$$

$$p_w \hat{\mathbf{W}} = \frac{qp_{q,x} + Qp_{Q,x}}{Q^2 + q^2} \begin{pmatrix} q\hat{\mathbf{x}} \\ Q\hat{\mathbf{X}} \end{pmatrix} \quad (\text{B15})$$

Equation B14 describes the A–BC bend, and eq B15 describes the rotational motion of the ABC molecule in the ABC plane. Note that whereas the momenta defined in eqs B8–B13 describe independent motion of either \mathbf{Q} or \mathbf{q} and are thus three vectors, the momenta defined in eqs B14 and B15 describe concerted motion of both \mathbf{Q} and \mathbf{q} and are six vectors. The momentum described in eq B14, for example, is a combination of the motion of \mathbf{q} along $\hat{\mathbf{x}}$ with a magnitude of $Q[(Qp_{q,x} - qp_{Q,x})/(Q^2 + q^2)]$, and the motion of \mathbf{Q} along $-\hat{\mathbf{X}}$ with a magnitude of $q[(Qp_{q,x} - qp_{Q,x})/(Q^2 + q^2)]$.

We then write

$$\mathbf{p}_{\text{vib}} = p_{Q,y} \begin{pmatrix} 0 \\ \hat{\mathbf{Y}} \\ 0 \end{pmatrix} + p_{q,y} \begin{pmatrix} \hat{\mathbf{y}} \\ 0 \\ 0 \end{pmatrix} + \frac{Qp_{q,x} - qp_{Q,x}}{Q^2 + q^2} \begin{pmatrix} Q\hat{\mathbf{x}} \\ -q\hat{\mathbf{X}} \end{pmatrix} \quad (\text{B16})$$

and

$$\mathbf{p}_{\text{rot}} = p_{Q,z} \begin{pmatrix} 0 \\ \hat{\mathbf{z}} \\ 0 \end{pmatrix} + p_{q,z} \begin{pmatrix} \hat{\mathbf{z}} \\ 0 \\ 0 \end{pmatrix} + \frac{qp_{q,x} + Qp_{Q,x}}{Q^2 + q^2} \begin{pmatrix} q\hat{\mathbf{x}} \\ Q\hat{\mathbf{X}} \end{pmatrix} \quad (\text{B17})$$

Generalization to collinear geometries is straightforward. For collinear geometries, $\hat{\mathbf{y}} = \pm \hat{\mathbf{Y}}$. We pick two arbitrary unit vectors, $\hat{\mathbf{u}}$ and $\hat{\mathbf{v}}$, that are orthogonal to each other and to $\hat{\mathbf{y}}$ and $\hat{\mathbf{Y}}$. Then \mathbf{p}_q and \mathbf{p}_Q can be expressed in terms of these unit vectors as

$$\mathbf{p}_q = p_{q,u}\hat{\mathbf{u}} + p_{q,y}\hat{\mathbf{y}} + p_{q,v}\hat{\mathbf{v}} \quad (\text{B18})$$

$$\mathbf{p}_Q = p_{Q,u}\hat{\mathbf{u}} + p_{Q,y}\hat{\mathbf{Y}} + p_{Q,v}\hat{\mathbf{v}} \quad (\text{B19})$$

where

$$p_{q,u} = \mathbf{p}_q \cdot \hat{\mathbf{u}} \quad (\text{B20})$$

$$p_{q,y} = \mathbf{p}_q \cdot \hat{\mathbf{y}} \quad (\text{B21})$$

$$p_{q,v} = \mathbf{p}_q \cdot \hat{\mathbf{v}} \quad (\text{B22})$$

$$p_{Q,u} = \mathbf{p}_Q \cdot \hat{\mathbf{u}} \quad (\text{B23})$$

$$p_{Q,y} = \mathbf{p}_Q \cdot \hat{\mathbf{Y}} \quad (\text{B24})$$

$$p_{Q,v} = \mathbf{p}_Q \cdot \hat{\mathbf{v}} \quad (\text{B25})$$

For collinear geometries, there are four vibrational modes. Two of them are given by eqs B21 and B24, which describe the vibration of the BC diatom and the vibration of the A–BC bond, respectively. Using the forms of the momenta suggested by eqs B14 and B15, we define four new momentum components by taking linear combinations of the components defined in eqs B20, B22, B23, and B25:

$$p_{b_1} \hat{\mathbf{b}}_1 = \frac{Qp_{q,u} - qp_{Q,u}}{Q^2 + q^2} \begin{pmatrix} Q\hat{\mathbf{u}} \\ -q\hat{\mathbf{u}} \cos \chi \end{pmatrix} \quad (\text{B26})$$

$$p_{b_2} \hat{\mathbf{b}}_2 = \frac{qp_{q,u} + Qp_{Q,u}}{Q^2 + q^2} \begin{pmatrix} q\hat{\mathbf{u}} \cos \chi \\ Q\hat{\mathbf{u}} \end{pmatrix} \quad (\text{B27})$$

$$p_{b_3} \hat{\mathbf{b}}_3 = \frac{Qp_{q,v} - qp_{Q,v}}{Q^2 + q^2} \begin{pmatrix} Q\hat{\mathbf{v}} \\ -q\hat{\mathbf{v}} \cos \chi \end{pmatrix} \quad (\text{B28})$$

$$p_{b_4} \hat{\mathbf{b}}_4 = \frac{qp_{q,v} + Qp_{Q,v}}{Q^2 + q^2} (q\hat{\mathbf{v}} \cos \chi) \quad (\text{B29})$$

Note that $\cos \chi = \pm 1$ for collinear geometries.

We then write

$$\mathbf{p}_{\text{vib}} = p_{Q,y} \begin{pmatrix} 0 \\ \hat{\mathbf{y}} \end{pmatrix} + p_{q,y} \begin{pmatrix} \hat{\mathbf{y}} \\ 0 \end{pmatrix} + \frac{Qp_{q,u} - qp_{Q,u}}{Q^2 + q^2} (Q\hat{\mathbf{u}} - q\hat{\mathbf{u}} \cos \chi) + \frac{Qp_{q,v} - qp_{Q,v}}{Q^2 + q^2} (Q\hat{\mathbf{v}} - q\hat{\mathbf{v}} \cos \chi) \quad (\text{B16a})$$

and

$$\mathbf{p}_{\text{rot}} = \frac{qp_{q,u} + Qp_{Q,u}}{Q^2 + q^2} (q\hat{\mathbf{u}} \cos \chi) + \frac{qp_{q,v} + Qp_{Q,v}}{Q^2 + q^2} (q\hat{\mathbf{v}} \cos \chi) \quad (\text{B17a})$$

References and Notes

- (1) Preston, R. K.; Tully, J. C. *J. Chem. Phys.* **1971**, *54*, 4297.
- (2) Truhlar, D. G.; Duff, J. W.; Blais, N. C.; Tully, J. C.; Garrett, B. C. *J. Chem. Phys.* **1982**, *77*, 764.
- (3) Blais, N. C.; Truhlar, D. G. *J. Chem. Phys.* **1983**, *79*, 1334.
- (4) Blais, N. C.; Truhlar, D. G.; Mead, C. A. *J. Chem. Phys.* **1988**, *89*, 6204.
- (5) Tully, J. C. *J. Chem. Phys.* **1990**, *93*, 1061.
- (6) Stine, J. R.; Muckerman, J. C. *J. Phys. Chem.* **1987**, *91*, 459.
- (7) Herman, M. F. *J. Chem. Phys.* **1984**, *81*, 754.
- (8) Coker, D. F.; Xiao, L. *J. Chem. Phys.* **1995**, *102*, 496.
- (9) Topaler, M. S.; Allison, T. C.; Schwenke, D. W.; Truhlar, D. G. *J. Phys. Chem.* **1998**, *102*, 1666.
- (10) Topaler, M. S.; Allison, T. C.; Schwenke, D. W.; Truhlar, D. G. *J. Chem. Phys.* **1998**, *109*, 3321; **1999**, *110*, 687(E).
- (11) Eaker, C. W. *J. Chem. Phys.* **1987**, *87*, 4532.
- (12) Volobuev, Y. L.; Hack, M. D.; Schwenke, D. W.; Truhlar, D. G. *J. Phys. Chem. A*, submitted.
- (13) Müller, U.; Stock, G. *J. Chem. Phys.* **1997**, *107*, 6230.
- (14) Chapman, S. *Adv. Chem. Phys.* **1992**, *82*, 423.
- (15) Tully, J. C. In *Modern Methods for Multidimensional Dynamics Computations*; Thompson, D. L., Ed.; World Scientific: Singapore, 1998; pp 37–72.
- (16) Tully, J. C. *Faraday Discuss. Chem. Soc.* **1998**, *110*, 407.
- (17) Topaler, M. S.; Hack, M. D.; Allison, T. C.; Liu, Y.-P.; Mielke, S. L.; Schwenke, D. W.; Truhlar, D. G. *J. Chem. Phys.* **1997**, *106*, 8699.
- (18) Truhlar, D. G.; Hack, M. D.; Volobuev, Y. L.; Topaler, M. S. *Faraday Discuss. Chem. Soc.* **1998**, *110*, 491.
- (19) Katz, G.; Zeiri, Y.; Kosloff, R.; Topaler, M. S.; Truhlar, D. G. *Faraday Discuss. Chem. Soc.* **1998**, *110*, 21.
- (20) Zeiri, Y.; Katz, G.; Kosloff, R.; Topaler, M. S.; Truhlar, D. G.; Polanyi, J. C. *Chem. Phys. Lett.* **1999**, *300*, 523.
- (21) Hack, M. D.; Truhlar, D. G. *J. Chem. Phys.* **1999**, *110*, 4315.
- (22) Bischof, C.; Carle, A. ADIFOR, version 2.0, 1998.
- (23) Simons, J. *Energetic Principles of Chemical Reactions*; Jones and Bartlett: Boston, 1983.
- (24) Mielke, S. L.; Tawa, G. J.; Truhlar, D. G.; Schwenke, D. W. *J. Am. Chem. Soc.* **1993**, *115*, 6436.
- (25) Simons, J. *ACS Symp. Ser.* **1984**, *263*, 3.
- (26) Mielke, S. L.; Tawa, G. J.; Truhlar, D. G. *Int. J. Quantum Chem., Symp.* **1993**, *27*, 621.
- (27) Schwenke, D. W.; Truhlar, D. G. *J. Chem. Phys.* **1987**, *87*, 1095.
- (28) Hazi, A. U. *Phys. Rev. A* **1979**, *19*, 920.
- (29) Weidenmüller, H. A. *Ann. Phys. (N.Y.)* **1964**, *28*, 60.
- (30) Weidenmüller, H. A. *Ann. Phys. (N.Y.)* **1964**, *29*, 378.
- (31) Newton, R. G. *Scattering Theory of Waves and Particles*, 2nd ed; Springer-Verlag: New York, 1982.
- (32) Taylor, J. R. *Scattering Theory*; Wiley: New York, 1972.
- (33) Bohm, A. *Quantum Mechanics Foundations and Applications*, 3rd ed.; Springer-Verlag: New York, 1993.
- (34) Cohen-Tannoudji, C.; Diu, B.; Laloë, F. *Quantum Mechanics*; John Wiley and Sons: New York, 1977; Vol. 1, pp 337–340.
- (35) Tawa, G. J.; Mielke, S. L.; Truhlar, D. G.; Schwenke, D. W. In *Advances in Molecular Vibrations and Collisional Dynamics*; Bowman, J. M., Ed.; JAI: Greenwich, CT, 1994; Vol. 2B, pp 45–116.
- (36) Tawa, G. J.; Mielke, S. L.; Truhlar, D. G.; Schwenke, D. W. *J. Chem. Phys.* **1994**, *100*, 5751.
- (37) Schwenke, D. W.; Mielke, S. L.; Tawa, G. J.; Chatfield, D. C.; Sun, Y.; Haug, K.; Allison, T. C.; Friedman, R. S.; Volobuev, Y. L.; Zhao, M.; Halvick, P.; Hack, M. D.; Truhlar, D. G. vP, version 18.5; University of Minnesota, 1998.
- (38) Schwenke, D. W. *Comp. Phys. Commun.* **1992**, *70*, 1.
- (39) Klepeis, N. E.; East, A. L. L.; Császár, A. G.; Allen, W. D.; Lee, T. J.; Schwenke, D. W. *J. Chem. Phys.* **1993**, *99*, 3865.
- (40) See, e.g.: Temkin, A.; Bhatia, A. K. In *Autoionization: Recent Developments and Applications*; Temkin, A., Ed.; Plenum: New York, 1985; pp 1–34.
- (41) Press, W. H.; Teukolsky, S. A.; Vetterling, W. T.; Flannery, B. P. *Numerical Recipes in FORTRAN*, 2nd ed.; Cambridge University Press: Cambridge, 1994; pp 716–725.
- (42) Hammes-Schiffer, S.; Tully, J. C. *J. Chem. Phys.* **1994**, *101*, 4657.
- (43) Truhlar, D. G.; Muckerman, J. T. In *Atom-Molecule Collision Theory*; Bernstein, R. B., Ed.; Plenum: New York, 1979; pp 506–566.
- (44) Gordon, R. G. *J. Chem. Phys.* **1966**, *44*, 3083.
- (45) Blais, N. C.; Truhlar, D. G. *J. Chem. Phys.* **1976**, *65*, 5335.
- (46) Truhlar, D. G. *Int. J. Quantum Chem., Symp.* **1976**, *10*, 239.
- (47) Truhlar, D. G.; Reid, B. P.; Zurawski, D. E.; Gray, J. C. *J. Phys. Chem.* **1981**, *85*, 786.
- (48) Smith, F. T. *Phys. Rev.* **1960**, *118*, 349.
- (49) Duff, J. W.; Truhlar, D. G. *Chem. Phys.* **1974**, *4*, 1.
- (50) Tully, J. C. In *Modern Theoretical Chemistry, Part B*; Miller, W. H., Ed.; Plenum Press: New York, 1976.
- (51) Garrett, B. C.; Truhlar, D. G. In *Theory of Scattering: Papers in Honor of Henry Eyring*; Henderson, D., Ed.; Theoretical Chemistry: Advances and Perspectives 6A; Academic Press: New York, 1981.
- (52) Mead, C. A.; Truhlar, D. G. *J. Chem. Phys.* **1982**, *77*, 6090.